Real-Time Schottky Measurements in the LHC

Bachelor's thesis for electrical engineering

Author: Even WANVIK, CERN, BE-BI-SW
CERN Supervisor: D. Alves, CERN, BE-BI-SW
NTNU Supervisor: D. Aune, NTNU, Associate Professor at the Department of Engineering Cybernetic

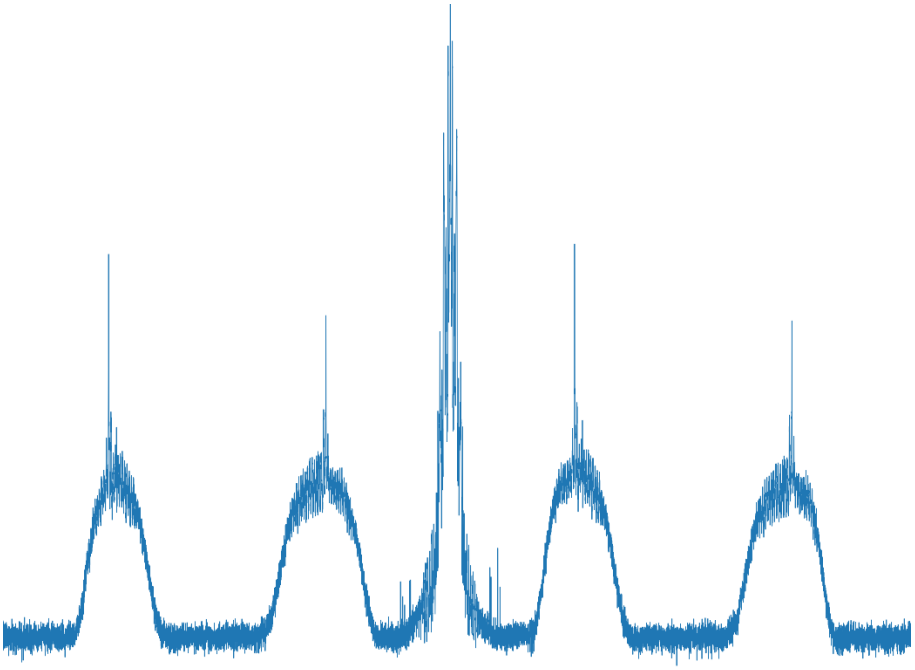

January 24, 2018
CH-1211 Geneva 23

The European Organization for Nuclear Research

The Norwegian University of Science and Technology
Faculty of Information Technology and Electrical Engineering (IE)
Department of Engineering Cybernetics

CERN-THESIS-2017-299
18/12/2017

Abstract

The accelerator complex at the European Organization for Nuclear Research (CERN) is a diverse collection of machines, tailored for different energy ranges, and concatenated in order to accelerate/decelerate particle beams. Leading up to CERN's flagship accelerator, the Large Hadron Collider (LHC), every accelerator in the chain boosts the particles to higher energies before they are injected into the next machine in the sequence. The LHC is a circular synchrotron accelerator consisting of two 27-kilometer vacuum tubes equipped with superconducting magnets and accelerating RF cavities in order to increase the energy of the particles along the way. Inside the vacuum tubes, two counter-rotating high-energy particle beams travel at velocities close to the speed of light before they are made to collide inside particle detectors at a centre-of-mass energy of 13 TeV.

As the particles are accelerated, they experience various external and internal forces. RF cavities are used to boost the speed of the particles and keep them in discrete bunches, dipole magnets are used to bend the particles into a circular orbit while some higher order magnets act as lenses that focus the beam. For ensuring the quality of the beam and controlling its stability, a set of important machine parameters need to be measured/estimated.

The LHC Schottky beam diagnostics system was designed with the intent of measuring important beam parameters such as tune, chromaticity, synchrotron frequency, momentum spread, etc. Compared to the presently available invasive methods that can cause significant particle losses, the LHC Schottky system is able to measure in a passive way. It does so by detecting internal statistical fluctuations of the beam particles, the so-called Schottky noise, and extracting the information that is encoded in the obtained frequency spectrum.

In this report we present the real-time implementation of the analysis of Schottky signals in the LHC. In particular, focusing on the measurement of the betatron tune, chromaticity and synchrotron frequency. **Chapter 1** provides insight into the history and evolution of a few significant accelerators while introducing the LHC accelerator chain. **chapter 2** introduces the physics of synchrotron accelerators and the importance of tune and chromaticity for beam diagnostics. **chapter 3** presents the theoretical background of the signals measured by Schottky systems. **chapter 4** introduces both the analog signal treatment chain and the implemented digital signal processes for the LHC Schottky system. **chapter 5** presents the real-time software that executes the digital signal processing steps introduced in the preceding chapter. In **chapter 6** the results of the implemented measurement methods and future work is discussed.

Acknowledgements

First of all, I would sincerely like to thank my CERN supervisor, Diogo Alves, whose selfless time and care were something that kept me going. His professional guidance and expertise have been more than helpful. He will forever have my sincere gratitude and respect. I wish him all the best in the future; he deserves the very best.

Next, I would like to thank all the wonderful staff members and students at the Faculty of Electrical Engineering at NTNU. Especially my supervisor Dag Aune and his colleagues during my specialization in electrical engineering and automatics for being outstanding lecturers.

Completing this work would have been all the more difficult were it not for the expertise and friendship of all members of my colleagues at the BE-BI-SW section.

Lastly, I would like to express my gratitude to my friends and roommates Nicholas Skram and Petter Krohg for several intellectual conversations, offering me advice and making my stay in Switzerland entertaining.

Acronyms

ADC	Analog-to-Digital Converter.
ALICE	A Large Ion Collider Experiment.
AM	Amplitude Modulated.
ATLAS	Argonne Tandem Linear Accelerator System.
BE	Beams Department.
CERN	European Organization for Nuclear Research.
CMS	Compact Muon Solenoid.
CMW	Controls Middleware.
DC	Direct Current.
DFT	Discrete Fourier transform.
DSP	Digital Signal Processing.
FEC	Front-End Computer.
FESA	Front-End Software Architecture.
FFT	Fast Fourier Transform.
FIR	Finite Impulse Response.
FODO	Focus-Drift-Defocus-Drift.
GUI	Graphical User Interface.
LHC	Large Hadron Collider.
LHCb	Large Hadron Collider beauty.
LINAC2	Linear Accelerator 2.
MD	Machine Development.
PLC	Programmable Logic Controller.
PS	Proton Synchrotron.
PSB	Proton Synchrotron Booster.
PSD	Power Spectral Density.
QD	Deocusing Quad.
QF	Focusing Quad.
r.m.s.	Root-Mean-Square.
RF	Radio Frequency.
SPS	Super Proton Synchrotron.

Symbols and Constants

Sign	Description	Unit
$B\rho$	Magnetic rigidity	Tm
B	Magnetic field	$T, \frac{Ns}{Cm}$
E	Energy, electric potential energy	J
L	The length or circumference of the accelerator	m
Q	Machine tune	–
α_c	Momentum compaction factor	–
β	Beta function, betatron amplitude	m
ϵ	Emittance - Area in plane occupied by beam particles	$m \cdot rad$
η	Slip factor	–
$\frac{\Delta Q}{Q}$	Relative tune	–
$\frac{\Delta p}{p}$	Relative momentum spread	–
γ	Gamma factor or Lorentz factor	–
ϕ	Initial angle of a particle.	rad
ψ	Betatron phase advance	rad
ρ	Accelerator radius	m
ξ	Correlation between tune deviations due to the relative momentum	–
c	Speed of light	$\frac{m}{s}$
$d(t)$	Dipolar moment. Describes the combination of transverse and longitudinal motion	–
e	Elementary charge	C
f_{rev}	Revolution frequency	s^{-1}, Hz
k	Field gradient	Tm^{-1}
k	Normalised field gradient	m^{-2}
p	Momentum or bessel order, easily seperated by context.	$\frac{kgm}{s}$
q	Fractional part of the tune	–
s	Longitudinal position	m
v	Velocity	$\frac{m}{s}$

Glossary

abstraction method of arranging the complexity of a computer system. It establishes different levels of complexity where an user interacts on a high level, while suppressing more complex details at lower levels..

back-end the data access layer of a piece of software, or inaccessible physical infrastructure or hardware..

beam stream of energized particles.

bunch discrete packets of particles.

calorimeter designed to stop particles as they pass thorugh the detector, measuring the amount of energy lost as each one grinds to a halt..

coupling phenomena where the planes affects one another, e.g. horizontal betatron motion is converted into vertical betatron motion and vice versa.

data field place where you can store data, commonly used to refer to a column in a database or a field in a data entry form or web form..

dipole moment combination of both longitudinal and betatron oscillations.

fill refers to filling the LHC with particles injected from the SPS. The fill number is incremented for every time the LHC is filled with "full" beams, just like filling a bottle.

front-end the part of the system the user interacts with.

harmonic number the harmonic numbers are the partial sums of the harmonic series. The n^{th} harmonic number is the sum of the reciprocals of each positive integer up to n.

JavaFX a software development platform from Oracle that is designed to facilitate desktop and rich internet applications (RIA) that can be accessed from a variety of devices.

kicker magnets that produce rectangular field pulses to excite or change the trajectory of the particles.

luminosity the ratio of the total detected collisions N within a time t at a cross-section (μ): $L = \frac{1}{\mu}\frac{dN}{dt}$.

magnetic lattice composition of electromagnets at given longitudinal positions around the accelerator.

phasor phase vector, a complex number representing a sinusoidal function..

photosensor sensors of light or other electromagnetic energy. A photo detector has a p–n junction that converts light photons into current..

PN-junction a boundary between p-type(positive, excess of "holes") and n-type(negative, excess of electrons) semiconductor material. Commonly used as diodes that allow flow of electricity in one direction in response to a applied voltage bias..

shotnoise noise from instinct transition effects of charged carriers.

synchronous particle reference particle ideally completely centered in the accelerator. optimally aligned with the longitudinal electric field from the RF cavities..

synchrotron type of accelerator where the accelerating particle beam travels around a fixed closed-loop path. The rate of acceleration is *synchronized* with the bending magnetic field.

thermal noise random fluctuations of electrons or holes in an electrical conductor with no DC current flow.

XML document (Extensible Markup Language) They are plain text files that don't do anything in and of themselves except describe the transportation, structure, and storage of data..

Contents

List of Tables

List of Figures

Chapter 1

CERN and accelerators

The accelerator complex at the European Organization for Nuclear Research (CERN) is a diverse collection of machines, tailored for different energy ranges, and concatenated in order to accelerate/decelerate particle beams. Leading up to CERN's flagship accelerator, the Large Hadron Collider (LHC), every accelerator in the chain boosts the particles to higher energies before they are injected into the next machine in the sequence (Fig. 1.1). Since Ernest Rutherford, in the early 20th century, prompted the invention of a particle accelerator, various accelerators with a wide range of machines have been invented. This chapter will provide a brief insight into the history and evolution of accelerators and introduce the LHC accelerator chain.

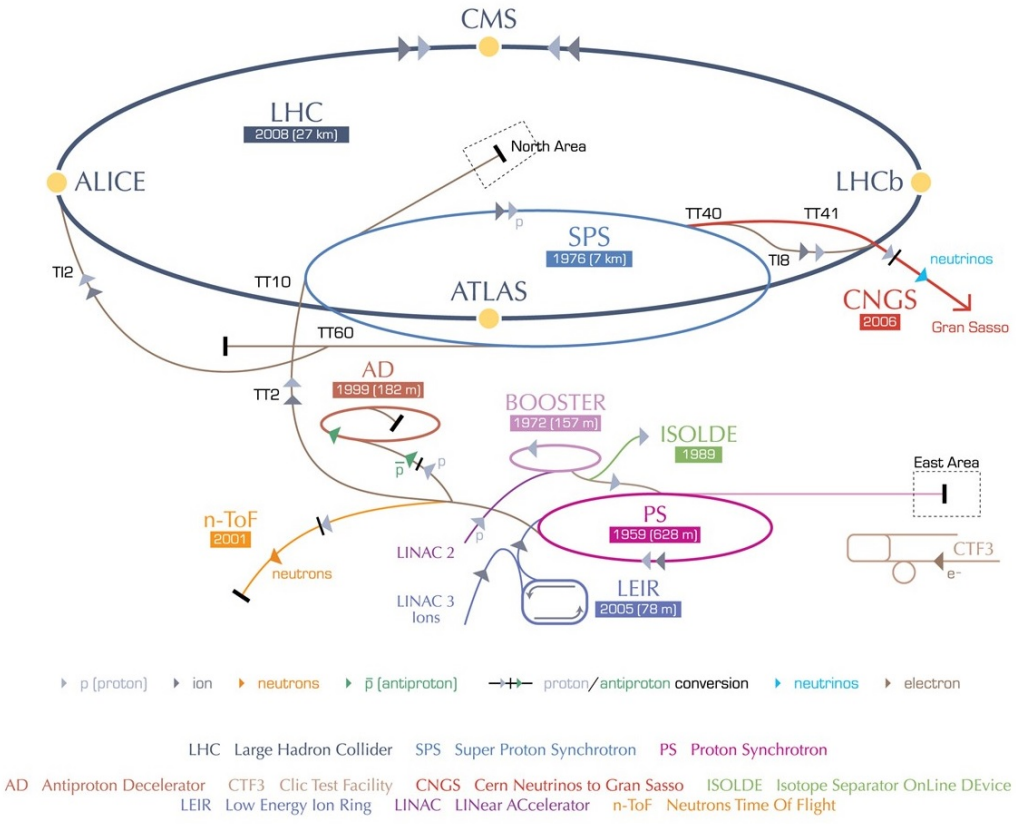

Figure 1.1: CERN accelerator complex

1.1 CERN

CERN was founded in 1954 and established in Geneva. Presently, CERN installations span the region around the French and Swiss border. The organization comprises 22 member states and more than 10,000 collaborator scientists from over 100 countries who probe, among other things, the fundamental properties and the origin of our universe. It is the home of some of the world's largest and most complex instruments. For instance, in the LHC, CERN's flagship accelerator, particles are accelerated and made to collide inside detectors (Fig. 1.1) at velocities close to the speed of light. The detectors gather clues about the particles - e.g. their speed, mass and charge - which process provides insight into the fundamental laws of nature and how the elementary particles decay and interact [2]. The data are collected by multiple layers of highly sensitive materials, which works like a huge camera that can study millions or even billions of particle collisions every second.

Every year hundreds of students come to CERN for training in research and engineering. With multiple applications from scientific research to everyday life, the technologies developed for particle physics have found applications in medical science, shaped the information technologies of today and pushed forward the frontiers of knowledge [3].

1.2 Types of accelerators and their legacy

High-energy physics research has always been the driving force behind the development of particle accelerators. What began in a small physics research laboratory, has long since outgrown this environment to become large-scale facilities. Accelerators can be very different, from mere meters to tens of kilometers and thousands to billions in value, with a wide range of applications. Only the most common and well-known accelerators will be presented in this short overview.

Electrostatic accelerator

The first particle accelerators to be exploited for nuclear physics research were electrostatic accelerators that used a static high voltage potential to accelerate a charged particle. Since opposites attract, a positive electric field will attract a negatively charged particle. The electrostatic accelerator is essentially a giant capacitor. This method is cheap and straightforward, but there is a limited amount of energy that can be transferred to a particle. After a while, the voltage will be at such a high level that the insulators will break. The first electrostatic accelerator built by two physicists, Ernest Walton and John Cockroft, in 1932.

Linear accelerator

The modern acceleration process utilizes oscillating electric fields for acceleration, first proposed by the Swedish scientist Ising in 1924, who planned to accelerate particles by applying an alternating voltage to create resonant electromagnetic fields. This is currently known as Radio Frequency (RF) acceleration and is the fundamental principle of present-day acceleration (more on this in chapter 2). The Norwegian physicist Rolf Widerøe built the first 'proof-of-concept' linear accelerator based on Ising's suggestion in 1928. He used a 1 MHz, 25 kV oscillator to make 50 keV potassium ions, using alternating drift tubes that are connected to the same terminal of an RF generator. The generator

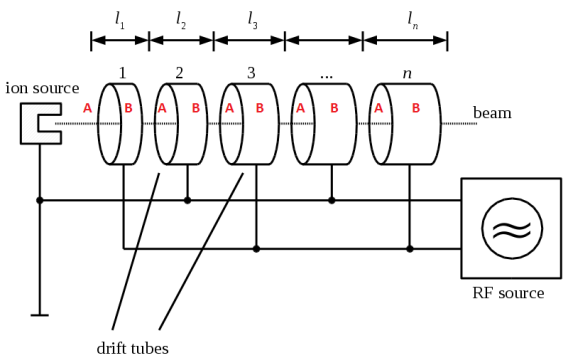

Figure 1.2: A schematic of Widerøe's linear accelerator

frequency is adjusted so that a particle crossing a gap sees an electric field in the direction of motion. When the particle is inside the drift tube, the field reverses so that the field attraction is in the desired direction at the next gap. As the particle gains speed, the gap between the tubes needs to be increased to maintain a constant acceleration.

The cyclotron

The linear accelerator was somewhat difficult to build, and during the 1930's it was pushed into the background by a simpler idea conceived by Ernest Lawrence in 1929, the fixed-frequency cyclotron (Fig. 1.3). It uses magnets to bend the moving particles in an almost circular motion between the acceleration passages. The RF section accelerates the particles as it passes from one 'dee' into the other. The particle is attracted to the positive 'dee' and the field changes polarity as the particle enters the other 'dee'. The frequency of the AC voltage must be equal to the revolution frequency in the cyclotron, which stays the same throughout the process while magnets keep the particles in a semicircular path, thus the beam tubes spiral shape. Ernest O. Lawrence's cyclotron was capable of delivering 20 MeV protons. The cyclotron, however, was limited in energy by relativistic effects (introduced in chapter 2) and despite the development of the synchrocyclotron, an original design was still required to reach yet higher energies. This new idea was the synchrotron (section 1.2).

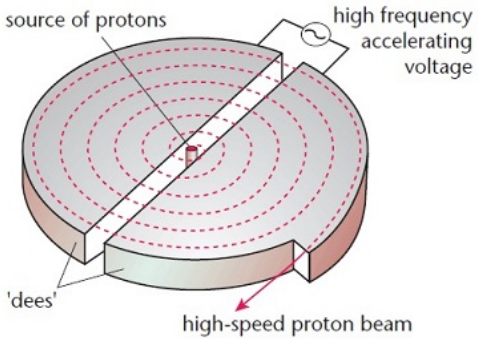

Figure 1.3: Image of a cyclotron. alternating voltage is applied to the 'dees' while a magnets keep the particles in a semi-circular motion.

The betatron

After its functionality, the betatron can be called a 'ray transformer' because it can be compared to a transformer where the secondary winding is replaced with a vacuum pipe where electrons can move freely. When entering the tube the electric field is increased, and the particle experiences an induced azimuthal e.m.f. [4] at the same time as they are deflected in an orbital motion because of the Lorentz force. If the magnetic field is correctly composed, they will be continuing in a circular motion while gaining speed and energy. The first betatron was built in 1940 by Kerst, but the principle it uses is based on Widerøe's annotations.

The Synchrotron

To accelerate particles at very high intensities, an accelerator needs mechanisms for focusing the beam in the transverse and longitudinal planes. The cyclotron is limited by relativistic effects, which cause the particles to lose synchronism (resonance) with the RF field (see section 2.1.2 and 2.3.3 in chapter 2). Without digging too deep into the physics, a longitudinal focusing mechanism is required. This problem was overcome in 1944 when E. McMillan and independently by soviet scientist V. Veksler discovered the principle of phase stability and invented the synchrotron [4]. Phase stability is when particles in the accelerator beam have a certain spread of energy and can be kept bunched throughout the acceleration cycle by simply injecting them at a suitable phase of the RF cycle of the receiving accelerator. An important footnote for the preceding sentence is that the beam in a synchrotrons is not a continuous string of particles, but is divided into tiny packets, what we refer to as bunches (the concept of bunching particles will be introduced in chapter 2, section 2.3.3). The first working synchrotron was built in 1946 by F. Goward and D. Barnes.

The acceleration principle is the same as the linear accelerator and cyclotron, using an RF voltage via a gap or cavity, except the particles are kept in a circular orbit by a dipolar magnetic

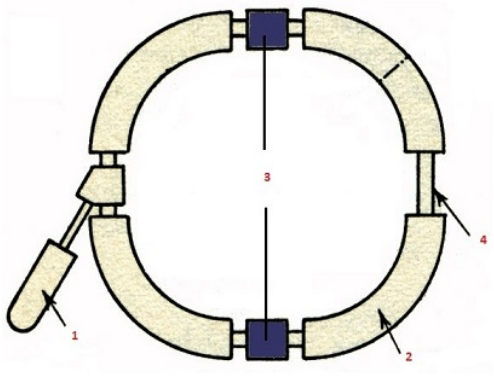

Figure 1.4: Injector(1), bending magnets(2), accelerating cavity(3), unaffected straight line(4).

field which is increased synchronously with the energy of the particle. The synchrotron is one of the first accelerator concepts to enable the construction of large-scale facilities, since bending, beam focusing and acceleration can be separated into different components. Theoretically, there are no limits to the energy that the particles can achieve in a synchrotron if the radius of the orbit or magnetic field bending the particles is big enough. There are, of course, physical and technological restraints that prohibit the construction of a purely theoretical and gigantic accelerator.

Other notable accelerators

Other accelerators worth mentioning is the microtron and the synchrocyclotron. The microtron is similar to the cyclotron, except that instead of having two D shaped parts it's a full circular container where particles are accelerated by a single cavity driven by an AC voltage. Under the influence of a magnetic field, the particle circulates back to the sole RF cavity that increases the energy and radius of the orbit. The synchrocyclotron is as the name implies a hybrid between a synchrotron and a cyclotron, built as a cyclotron but with the attribute of the synchrotron to overcome the relativistic effects. The synchrocyclotron differs from the classic cyclotron in that the frequency of the AC voltage is not kept constant, but is synchronized with the revolution frequency of the particles.

1.3 The LHC accelerator chain

Atoms (mostly hydrogen, but sometimes lead or xenon) are fed from a gas cylinder at a controlled rate into the source chamber of the Linear Accelerator 2 (LINAC2), as shown in Fig. 1.1 and as a simple schematic in Fig. 1.2. There the electrons are stripped off leaving only the nuclei, i.e. ions, which have a positive charge that enables them to be accelerated by an electric field. The initial acceleration provided by the LINAC2 can be associated with the first stage of a rocket. By the time the protons leave LINAC2, they will be traveling at one-third the speed of light, increasing energy levels from 0 to 50 MeV[1].

The second stage of the acceleration process occurs in the Proton Synchrotron Booster (PSB). This is the first and smallest circular (synchrotron) accelerator. It contains four superimposed rings with a circumference of 157 meters. The incoming particles are separated into four beams, one for each of the booster rings (Fig. 1.5). The four beams are accelerated by repeatedly being subject to a pulsed electric field while circulating the rings, the same way as you would continuously give a pendulum an extra push at a certain point in its fluctuations. As introduced in section 1.2 about synchrotrons, powerful electromagnets along the beam line exert a force

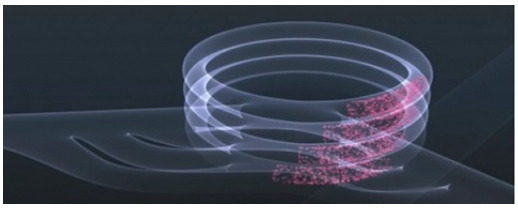

Figure 1.5: PSB (Proton Synchrotron Booster), the second component of the acceleration sequence. The incoming beam is divided into four, one for each superimposed ring.

[1]eV - unit of energy, 1 electron volt has the same energy as the elementary charge, usually denoted as e or sometimes q.

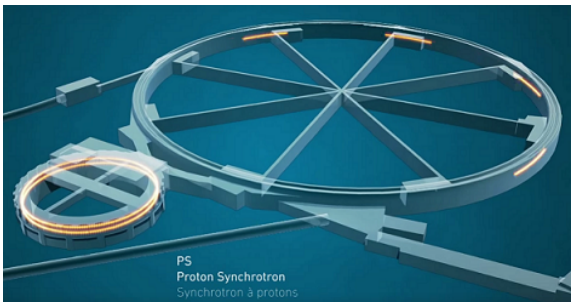

Figure 1.6: The PSB and PS, where the latter is the bigger of the two synchrotrons shown on the figure and the third component of the acceleration sequence.

at right angles to their direction of motion and are used to bend the beam of protons around the circle. The PSB accelerates the particles up to 98.6 percent the speed of light, increasing energy levels from 50 MeV to 1.4 GeV and squeezes them closer together.

After recombining the beam again, they are flung into the Proton Synchrotron (PS), which is stage three of the acceleration chain and is 628 meters in circumference. Although the particles only spend 1.2 seconds on this stage, it manages to reach 99.9 percent the speed of light, increasing energy levels from 1.4 to 25 GeV. This is a transition point for the beam, as it enters the regime of special relativity. Added energy from a pulsating electric field can no longer be converted into an increase in velocity since they are already approaching the universal speed limit. The added energy after this transition converts into an increase in mass, more on this in section 2.1.2.

The beam of particles is now directed to stage four, the Super Proton Synchrotron (SPS), a large ring 7 kilometers in circumference. It is designed explicitly for protons, whereas the earlier stages are more versatile and can accelerate protons, antiprotons, electrons, positrons and other classes of ions. The SPS increases the energy of the beam from 25 GeV to 450 GeV. After 1.2 seconds on this stage, the packets are sufficiently energized to be launched into the orbit of the gigantic LHC.

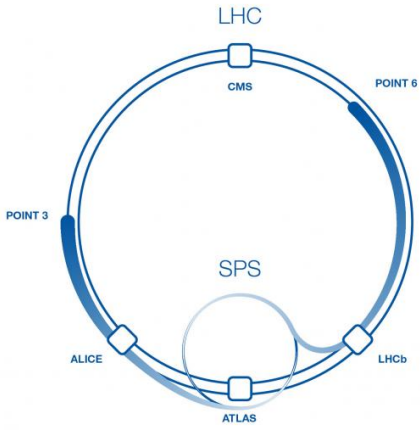

Figure 1.7: The SPS and LHC, respectively the fourth and last of the accelerators.

There are not one, as for the other accelerators, but two vacuum beam pipes within the LHC, containing beams traveling in opposite directions. Using a sophisticated kicker system the beam bunchs from the SPS are separately propagated into two pipes in different directions, i.e. clockwise and counterclockwise. These counter-rotating beams cross over in the four detector caverns; Argonne Tandem Linear Accelerator System (ATLAS), A Large Ion Collider Experiment (ALICE), Compact Muon Solenoid (CMS) and Large Hadron Collider beauty (LHCb) (Fig. 1.9), where they can be made to collide with each other. The energy of the collision is twice that of the opposing proton beams, and it is the collision debris that is tracked in the detector. For about half an hour the SPS produces bunches that are being injected into the LHC, which finally accumulates

to 2808 bunches circulating the accelerator [5]. During the LHC's acceleration cycle the energy levels will be increased from 450 GeV to at most 7 TeV. The particles circulates the 27-kilometer accelerator ring over 11,000 times a second, with a revolution frequency equal to 11.2455 kHz to be precise. The velocities during a complete injection to collision cycle are so close to the speed of light that the particles will be 7000 times more massive than at rest as a consequence of special relativity (section 2.2). The magnetic force necessary to keep the curvature of the beam along the ring is now so enormous that the main bending magnets use a current of 11,080 amperes to generate powerful 8.3 tesla magnetic fields - more than 100,000 times more powerful than the Earth's magnetic field [6]. This is achieved by making the LHC colder than outer space so that its magnets becomes superconducting. After reaching stable beams at 6.5 TeV, they are ready to collide in the detectors [7].

Figure 1.8: Lying deep under ground (122m to lowest point), the LHC has a 27 kilometers circumference. It lies between the Jura mountains and the Alps, covering both French and Swiss soil.

LHC vital statistics

Particles used: Protons and heavy ions (Lead and Xenon)

Circumference: 26,659 m

Injector: SPS

Injected beam energy: 450 GeV

Nominal beam energy in physics[2]: 7 TeV (protons)

Magnetic field at 7 TeV: 8.33 Tesla

Operating temperature: 1.9 K

Number of magnets: 9300

Number of main dipoles (section 2.2.1): 1232

Number of quadrupoles (section 2.2.2): 858

Number of correcting magnets (section 2.2.2): 6208

Number of RF cavities: (section 2.3.3: 8 per beam; Field strength at top energy $\approx$ 5.5 MV/m

RF frequency: 400.8 MHz

Revolution frequency: 11.2455 Khz

Power consumption: 120 MW

Gradient of the tunnel: 1.4

Difference between highest and lowest points: 122 m

For more information on the essential LHC statistics and parameter check out the "LHC Design Report" [5].

[2] 'Physics beam' or 'phsyics run' - Referring to stable beams customized for collision

1.4 LHC experiments

There are a total of seven experiments at the LHC used to analyze the endless amount of particles produced by collisions in the accelerator. Each experiment is unique and defined by its detectors. The bigger of the seven experiments, ATLAS and CMS, have more general-purpose detectors, that cross-validate the results leading up to new discoveries. ALICE and LHCb have specialized detectors that focus on specific phenomena. The other three experiments concentrate on non-colliding-particles events but are less necessary for the accelerator context.

Each of the particle-colliding detectors is like a huge camera that can study millions or even billions of particle collision in one second. A steering magnet brings the protons on a collision course in the cross-section, where the detector caverns are located. The total energy of two protons colliding in the LHC is at most 14 TeV. The energy of the collisions are so high that particles erupt into existence and leaves a path of light. Dense layers of calorimeter picks up these energy deposits from the collision debris and creates a complete image of the particle's trajectory and energy. The data collected at the experiments are shared with scientists from institutes all over the world [8; 2].

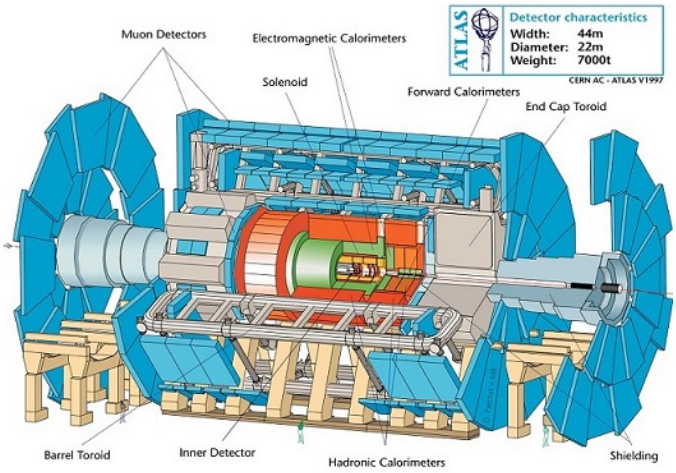

Figure 1.9: ATLAS is the world's largest general-purpose particle detector. It investigates a wide range of physics, from the search for the Higgs-boson to extra dimensions and particles that could make up dark matter.

Chapter 2

Synchrotron accelerator physics

To understand the nature of the measured Schottky signals in the LHC, one has to understand the basics of accelerator physics. This chapter will provide the necessary knowledge before introducing the concepts of the Schottky measurement system.

As particles are accelerated, they experience various external and internal forces. RF cavities are used to boost the particles and keep them in discrete bunchs; dipole[1] magnets preserves the particles in a circular orbit around the accelerator; higher order magnets act as lenses that focus the beam of particles, gathering the particles closer together.

A few important beam parameters will be introduced, for instance: momentum spread, tune, synchrotron and betatron frequency, chromaticity and emittance. All of these are essential and observable parameters that are crucial for estimating, measuring and controlling the beam stability in the LHC and other accelerators. Although a few equations will be introduced, the goal will not be to gain any deep and complex understanding of the physics or mathematics.

2.1 Prerequisites

In accelerator physics it's important to establish a convenient convention for a coordinate system in order to be able to represent the dynamics of the particles in both the longitudinal and transverse planes. This will be briefly addressed in section 2.1.1. In many modern accelerators, particles travel at speeds close to the speed of light. It is well known that relativistic effects can no longer be explained using Newtonian physics hence special relativity is required. In section 2.1.2 we will cover the basics of special relativity.

2.1.1 Coordinate system

To perceive the position and movement of the particles in the accelerator, it is essential to have a 3-D coordinate system for visualization. Using the coordinate system in Fig. 2.1, **x** is the horizontal transverse axis, **y** is the vertical transverse axis and **s** is the longitudinal axis. **θ** can also be used for the longitudinal phase advance in one revolution, i.e. from 0 to 2π.

What we call bunches are a collection of a very large numbers of particles[2] that have a finite energy spread with a center of mass that is moving in a well-defined orbit that passes through the center of the focusing elements of the machine following the circular black line in Fig. 2.1.

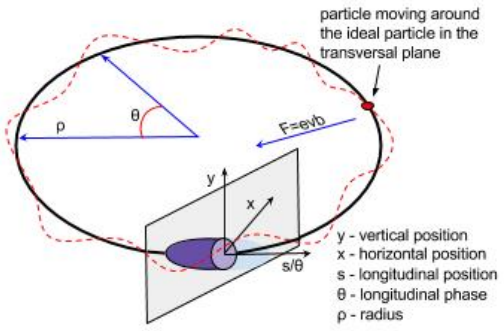

Figure 2.1: Reference coordinate system

[1] in *dipole*, *di* refers to the number of poles (2), e.g. higher order magnets might be *quadrupoles*, *sextupoles*, etc.
[2] in the LHC the number of particles in a nominal bunch is $\approx 10^{11}$ [5]

2.1.2 Special relativity

As a particle is accelerated from rest, it will quickly gain speed until it eventually approaches the speed of light c. As it approaches this universal speed limit, an increase in particle energy will progressively be converted into extra mass rather than extra velocity. At lower energy levels (lower velocities in Fig. 2.2) the speed of the particle is far from the speed of light, and traditional Newtonian mechanics defines its motion. At the higher end of the energy spectrum, however, the particles enter the regime of special relativity. This implies we need a different set of laws to explain the particle's motion.

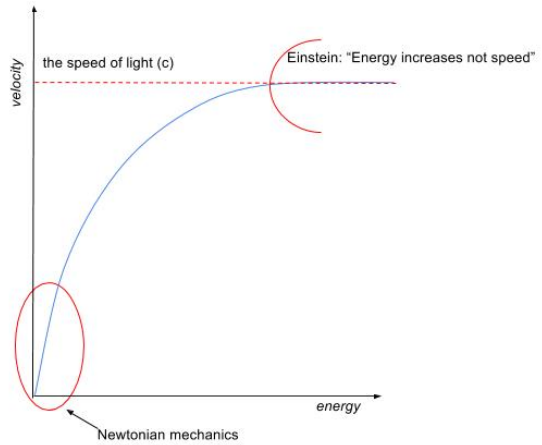

Figure 2.2: A particle's velocity as a function of energy. For instance in the LHC, the particle speeds are so close to the speed of light that special relativity governs the particle's dynamics.

The following are definitions that define the energy of any moving particle:

$$\text{Energy of a particle at rest: } E_0 = m_0 c^2$$

$$\text{Energy of a moving particle: } E = \gamma E_0 = \gamma m_0 c^2$$

To describe relativity we use the Gamma factor, also called the Lorentz factor γ which is given by the formula:

$$\gamma = \frac{1}{\sqrt{1 - v^2/c^2}} = \frac{1}{\sqrt{1 - \beta^2}} \ , \tag{2.1}$$

where v is the particle's velocity, c is the speed of light and $\beta = v/c$ the ratio between the particle's velocity and the speed of light (the relativistic beta). For a highly relativistic particle γ is large, i.e. the total energy is much larger than the rest energy, and the ratio between velocity and the speed of light $\beta \Rightarrow 1$. We can also see that β represents the ratio between momentum and the energy of a particle:

$$\beta = \frac{v}{c} = \frac{mv}{mc} = \frac{mvc}{mc^2}, \quad p = mv, \quad E = mc^2 \quad \Rightarrow \quad \beta = \frac{pc}{E} \ , \tag{2.2}$$

where the energy of the particle is given by $E = mc^2$ since the velocity is roughly the speed of light. For highly relativistic particles $\beta \approx 1$ and we can now say that $p = \frac{E}{c}$. This implies that for highly energetic particles, energy and momentum are numerically equal if momentum is expressed in units of Energy per c.

These are some minor but necessary conclusions that will be applied in the coming chapters, as most of the examples used herein will consist of dynamics in the special relativity regime. Section 2.3.1, dealing with high energy longitudinal motion, will elaborate more on the topic of special relativity.

2.2 Transverse beam dynamics

The LHC Schottky system is mainly focused on transverse beam diagnostic purposes. This section will provide necessary knowledge of the transverse dynamics and diagnostics of the particle beams before introducing the Schottky signals in the next chapter. Dipoles, quadrupoles and other higher order magnets will be introduced. A few vital parameters that can be measured and controlled for monitoring the beam behaviour in the transverse planes will also be presented.

2.2.1 Dipoles

For simply keeping the particles in a certain orbit, a powerful magnetic field is needed, which in the LHC and other circular accelerators is generated by the dipole magnets. The bending radius is defined by the particle momentum and the strength of this dipole field. The force on a charged particle e in a magnetic field of strength B, moving with a velocity v will be equal to the force $mass \times acceleration$ towards the center of its orbit (Lorentz force, discarding the accelerating electric field E [9]).

$$F = evB = \frac{mv^2}{\rho} \tag{2.3}$$

The latter is the equation for centripetal force, where ρ is the distance from the center and v the velocity vector perpendicular to the force vector (Fig. 2.3). If we now modify the equation by using the momentum $p = mv$, we get:

$$B\rho = \frac{mv}{e} = \frac{p}{e} \ . \tag{2.4}$$

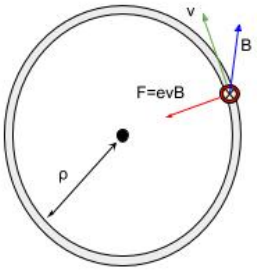

Figure 2.3: Motion of a particle in a dipole, the dipole magnetic field is illustrated as in/out of the page

ρ is a fixed value given by the accelerator's size and layout of its magnets. The magnetic field B and radius ρ compose something called "magnet rigidity" ($B\rho$). Eq. 2.4 tells us that as the momentum p increases, the magnetic field B has to follow. The formula for magnetic rigidity demonstrates the clear trade-off between the bending magnetic field B and its radius ρ when constructing an accelerator.

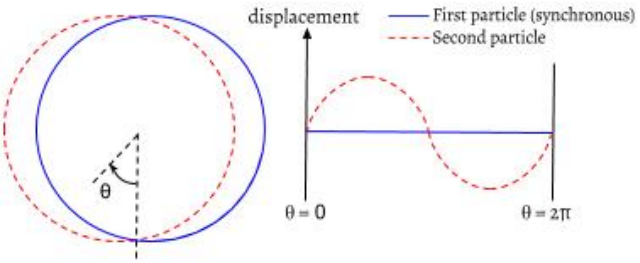

Figure 2.4: Betatron oscillations, the basis of all movement in the transversal plane.

Let us consider one of the transverse planes, for instance the horizontal (x) plane, and add two particles to the accelerator, both with different initial angles. Fig. 2.4 shows the trajectories for two arbitrary particles in a dipole field, with different initial horizontal angles. If we were to unfold these orbits into a "straight line" and plot the horizontal displacement of first particle with respect to the second, we would be able to see that the second particle oscillates around the first particle. This is the betatron oscillation and it forms the basis of all transverse motion in an accelerator [10].

2.2.2 Quadrupoles

If we now look at the betatron oscillations in both planes, we get a spiral that never closes. To force the particles closer toward the ideal orbit, some extra focusing in addition to the dipoles is necessary. This focusing force is achieved with quadrupole magnets and other higher order magnets[3].

The quadrupole magnet and the other higher order magnets can be considered as "thin lenses" and the beam as a diverging light beam (Fig. 2.5). The composition of electromagnets at a given position along the enclosed beam is referred to as the magnetic magnetic lattice. We have two types of quadrupoles; Focusing Quad (QF) and Deocusing Quad (QD). The QF focuses the beam in the horizontal plane and defocuses the beam in the vertical plane. Correspondingly if we rotate the QF 90 degrees it would become a QD, which has the opposite focusing attributes as the QF. A magnetic cell (designated locations equipped with magnets) will have a series of dipoles that keeps the particles in a closed longitudinal orbit, while QD and QF quadrupoles will constrain them in the transverse planes.

The composition of electromagnets along the path of the enclosed particle beam is called the magnetic magnetic lattice. Different magnetic lattice cells are repeated several times around the ring and lead to periodically repeated focusing properties. One of the most widespread magnetic lattice cells is the so-called Focus-Drift-Defocus-Drift (FODO) cell, a magnet structure consisting alternately of QF and QD quadrupole lenses shown to the left in Fig. 2.5.

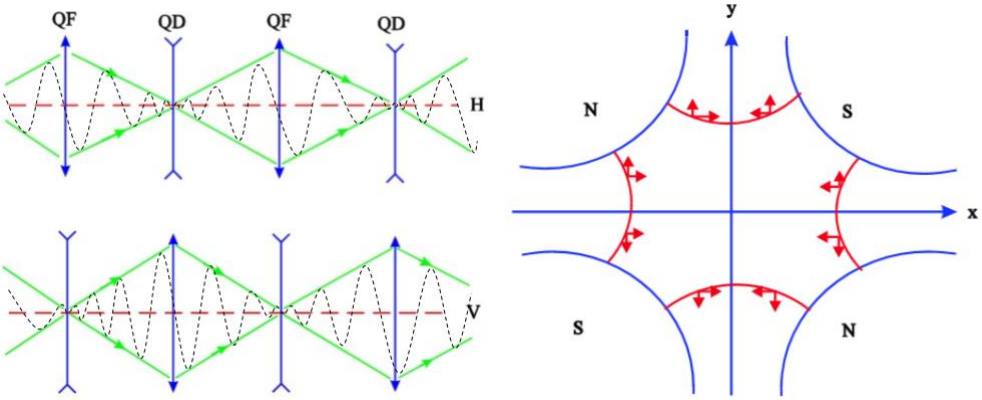

Figure 2.5: Left: Particle demonstrating betatron oscillations in focus (QF) and defocusing (QD) quadrupole magnets. Right: Force on a particle moving through a focusing quadrupole (QF). H is the horizontal x-axis on our coordinate system, while V is the vertical y-axis.

Looking at the magnetic field on the right-hand side in Fig. 2.5, there is no field along the central axis, but as we move along the x-axis (horizontally) the gradient field is vertical and vice versa. Maxwells equation given by [11]:

$$\nabla \times B = 0 \Rightarrow \frac{dB_y}{dx} - \frac{dB_x}{dy} = 0 \Rightarrow \frac{dB_y}{dx} = \frac{dB_x}{dy} \tag{2.5}$$

tells us that a particle that deviates from the central axis of the QF in the horizontal plane will be deflected back towards the center of the magnet.

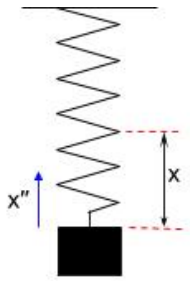

Figure 2.6: A Weighted spring with acceleration x'' and displacement x is a simple analogy to betatron oscillations in one plane

A general equation for transverse motion in an accelerator is given by Hill's equation [10]. In the horizontal plane this is given as:

$$\frac{d^2x}{ds^2} + K(s)x = 0 \tag{2.6}$$

The difference between Eq. 2.6 and for instance the equation for a weighted spring (Fig. 2.6), is that the spring constant k is not a constant and is a periodic function of the focusing strength of the magnetic lattice and t is replaced

[3] sextupole, octupole and decapole magnets, which correct for small imperfections in the magnetic fields

with the longitudinal position s encircling the accelerator. Eq. 2.6 can be expanded for horizontal and vertical terms as

$$\begin{cases} \ddot{x} + \left(k(s) + \frac{1}{\rho^2(s)}\right) \cdot x & = \frac{1}{\rho(s)} \frac{\Delta p}{p} + f_x(s,t) \\ \ddot{y} - k(s) \cdot y & = 0 + f_y(s,t) \end{cases} , \tag{2.7}$$

where $\rho(s)$ is the local bending radius of the dipoles,

$$k(s) = \frac{e}{p} \cdot \frac{dB}{dx} = \frac{dB/dx}{B\rho} = -\frac{dB/dy}{B\rho} \tag{2.8}$$

the normalized local quadrupole strength, $\frac{\Delta p}{p}$ the particle's relative momentum spread with respect to the ideal particle, and $f_{x,y}(s,t)$ is other sources of perturbation to the particle's motion. Eq. 2.8 for quadrupole strength $k(s)$ combines the equation for magnetic rigidity (Eq. 2.4) and quadrupole gradient field relations Eq. 2.5, which tells us that positive quadrupole strengths $k(s)$ in one plane essentially corresponds to the opposite in the other [12].

2.2.3 Phase space and emittance

The amplitude and frequency of the particles in the transverse planes are determined by the strength and outline of the magnetic magnetic lattice. Just like a shorter thread on a pendulum will decrease the amplitude but increase the frequency and vice versa, the same is true for the amplitude modulation of the particles behavior in the transverse planes. To resolve the transverse motion, three parameters will be introduced: ϵ, $\beta(s)$ (not to be confused with the ratio between velocity and the speed of light in 2.1.2) and $\psi(s)$, all of which represents the behavior of the beam with respect to the initial conditions (just after injection of particles) and the focusing strength of the quadrupoles and other higher order magnets. How a momentum change (acceleration) affects the transverse motion will be discussed later in this section. Imagine a solution for the horizontal plane, x, of the form

$$x = \sqrt{\epsilon\beta(s)} cos(\Psi(s) + \phi) \ ,$$

where the emittance ϵ and the initial phase ϕ are constant [10]. The beta function $\beta(s)$ is, in this case, a simple amplitude modulation due to the changing focusing strength (a more extensive version of the betatron function will appear later in section 2.2.4). $\Psi(s)$ is the phase advance, which also depends on focusing strength.

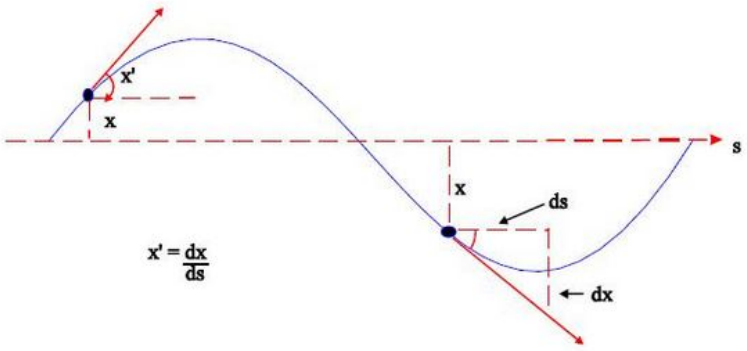

Figure 2.7: Betatron oscillation in the horizontal plane. The position of the proton in the transverse planes are characterized by two things: the position or displacement (x) and angle (x') with respect to the central path.

As previously mentioned, it is obvious that decreasing amplitude increases the frequency and vice versa. This relationship then leads to the conclusion that the rate of change in phase for the betatron oscillation throughout the ring is proportional to the inverse of the particle's amplitude $d\Psi(s)/ds = 1/\beta(s)$ [10]. If we calculate the particle's angle x' from the already established β function:

$$\text{angle} = x' = \frac{dx}{ds} = -\sqrt{\epsilon\beta(s)} \frac{d\Psi(s)}{ds} sin(\Psi(s) + \phi) = -\sqrt{\frac{\epsilon}{\beta(s)}} sin(\Psi(s) + \phi) \ ,$$

and plot the values for the function over many turns at a specific position s about the accelerator, where the betatron function $\beta(s)$ is constant, we get something like the phase space plot shown on Fig. 2.8. ϵ is called the emittance and is for now determined solely by initial conditions, i.e. the conditions of the beam as it was injected from the previous accelerator (in the LHC the particles are injected from the SPS). The beta function β however, varies as a function of the magnetic magnetic lattice around the accelerator. But since the amplitude and phase advance depends on the inverse $\beta(s)$ of one another and emittance is constant, the area of the ellipse remains constant throughout the accelerator. If we now were to measure the position of every particle, with different β functions, at a single position in one revolution of the accelerator and plot them, we would see the whole area inside figure 2.8 being filled with black dots. The correct definition of the emittance is that it is the area of the ellipse which contains a certain percentage of the particles, i.e. a "100%" emittance contains all the particles, "95%" ..., etc.

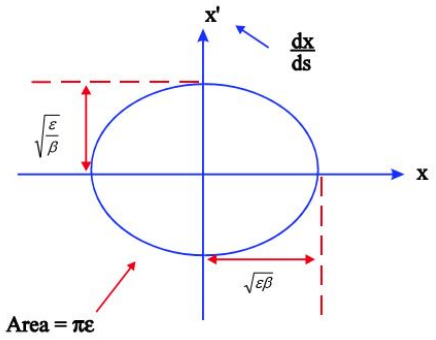

Figure 2.8: Transverse phase space plot for a single particle

The projection of the ellipse in Fig. 2.8 onto the x-axis will give the horizontal size of the beam. Using a $\beta(s)$ as a changing focusing strength for each of the planes as illustrated in Fig. 2.5 we can imagine the beam changing shape as each plane alternate between focusing or defocusing cells. As already stated, the total emittance is determined by the initial conditions, and the variation in the beam envelope is determined by the changing $\beta(s)$ of each plane. This means that the beam size stays the same, but its shape in each plane will more or less follow the green tangent line in Fig. 2.5.

Emittance ϵ has units of length, but can be referred to as "$length \times angle$" (Fig. 2.8). The Emittance is measured in all three dimensions, i.e. longitudinal emittance (section 2.3.3), horizontal emittance, or vertical emittance (latter two is collectively be referred to as transverse emittance). Until now only the emittance just after injection has been the case, but in reality, it changes as a function of the beam momentum: increasing the energy of the beam (accelerating the beam) reduces the emittance [10].

2.2.4 Tune and perturbation sources

The number of betatron (transverse motion) oscillations that are performed by the particles in one revolution of the accelerator is denoted as the "tune" or Q-value. Still using ψ as the betatron phase advance of the particle, tune can written as

$$Q := \frac{1}{2\pi} \int_L \psi(s) ds, \tag{2.9}$$

where L is the circumference of the accelerator. The tune is split into two pieces, an integer part Q_{int} and non-integer (fractional) part denoted by q_{frac}, or just q:

$$Q = Q_{int} + q \tag{2.10}$$

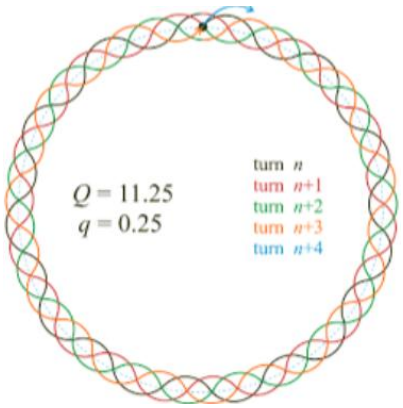

Figure 2.9: Tune with a fractional part that excites 4th order resonance, after 4 revolutions the particle is lost in the accelerator (black dot).

A collection of the diagnostics devices and methods in the LHC, including the Schottky system, measure the fractional part of the tune. It is a crucial parameter for the accelerator's performance, which will be made apparent in this section. Imagine that a particle performs 11.25 horizontal betatron oscillations, i.e. in the horizontal plane (we have both horizontal tune and vertical tune), in one revolution. This gives it a integer part of $Q_{h,int} = 11$ and a fractional part of $q_h = 0.25$, as used in Fig. 2.9. After 11.25 horizontal betatron oscillations, the particle is at the same point (marked as a black dot in Fig. 2.9) as it started. The particle will have a different transverse position each time it reaches the same position as the black dot after each revolution. If we now include a magnet error at this exact location, the particle will feel a

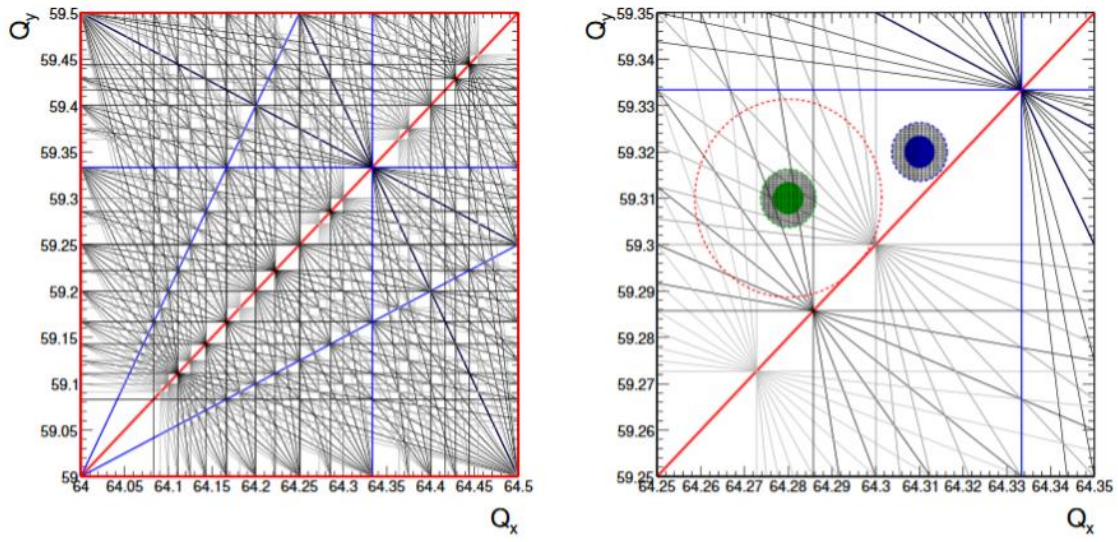

(a) Full tune diagram (b) Zoom around LHC Q working points

Figure 2.10: Full tune diagram showing up to twelfth order resonances (a) and zoomed to the LHC tune working point (b). First and second order resonance lines are plotted red, third is plotted blue, and the higher orders with increasingly brightening shades of grey. The LHC injection (green: ($q_x = 0.28$, $q_y = 0.31$) and particle collision (blue: $q_x = 0.31$, $q_y = 0.32$) tune working points are indicated [5]. Inside the round solid colored circles is the most effective estimated tune, the intermediate grey circles is the tolerance margins, and the red dotted outer circle describe the maximum allowed tune tolerance, but the last one only tune resonance.

deflecting force every time it passes. The fractional part of the tune q_h will cause the particle to be in the same horizontal position at this deflection source every fourth turn and the particle will eventually be lost in the accelerator because of this deflection. This is called a 4th order resonance. Most of the lower order resonances originate from storage ring magnets; dipoles excite 1st order resonances; quadrupoles excite 2nd and 4th order resonances; sextupoles excites both 1st and 3rd order resonances; octupoles excites both 2nd and 4th order resonances; Decapole ... etc [10]. In order to avoid these deflection feedbacks caused by machine imperfections such as magnetic errors, the tune is ideally kept at an irrational number (Fig. 2.10). In addition the horizontal and vertical tune usually differ in order to avoid coupling resonances between planes. As an example the horizontal tune at collision energy (6.5 TeV) is supposed to be 64.31, while the vertical tune is set as 59.32 [5]. Fig. 2.10 shows a diagram of resonances up to the 12th order, with decreasing shade of grey for higher orders.

There is a collection of tune perturbation sources, some of which, like the magnetic errors, may be identified and compensated for during maintenance periods. To uphold appropriate tune tolerance levels, beam measurements, automatic diagnostics and control of the tune is needed. A quick list of some of the most critical perturbation sources [12]:

- Magnetic field errors due to for, for instance, saturation of iron yoke, calibration errors, power converter ripples, saturation of the magnet, etc.
- momentum shifts due to, for instance, different reference momenta between dipole and quadrupole magnets, energy mismatch between injection and current storage ring energy.
- feed-down errors from the other higher order magnets.

Most tune perturbations is derived from quadrupole field errors, which is described in ref [10] as:

$$\Delta Q = \frac{1}{4\pi}\beta(s) \cdot \Delta k(s) \ , \tag{2.11}$$

where $\beta(s)$ is the betatron function (was introduced in section 2.2.3 and is thoroughly explained in [12]), which defines the betatron oscillations and consequently the transversal size of the beam

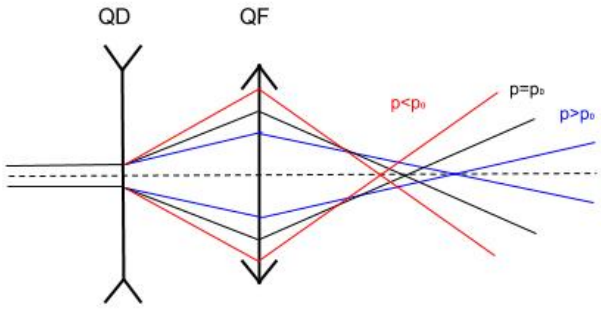

Figure 2.11: Quadrupole's focusing strength dependence on particle momentum

and the focusing strength $k(s)$ of the quadrupole from Eq. 2.8. This error can be summed up for every quadrupole error around the accelerator. From Eq. 2.11 it is visible that a greater betatron amplitude $\beta(s)$ or quadrupole gradient $k(s)$ will induce a larger tune shift ΔQ.

Another tune perturbation source that is important to note is if the particle's momentum does not match the design of the quadrupole magnet(Fig. 2.11). If we now expand the term for focusing strength from Eq. 2.8 by replacing p with the momentum error $p_0 + \Delta p$ using a Maclaurin series (Eq. (3,34) [13]) $1/p = 1 - p + p^2 +$ h.o. (higher order terms) and do the partial derivatives of z as a function of x and y we get the quadrupole field gradient:

$$k(s) = \frac{e}{p}\frac{\partial B}{\partial z} = k_0(s) - k_0(s) \cdot \frac{\Delta p}{p} + k_0(s) \cdot \left(\frac{\Delta p}{p}\right)^2 + \text{h.o. } ... \tag{2.12}$$

The series from Eq. 2.12 can now be inserted into Eq. 2.11. Applying an integral over the closed line of the accelerator L to get the total tune shifts as a consequence of the quadrupole errors:

$$\Delta Q = \frac{1}{4\pi} \oint_L \beta(s) k(s)\, ds \cdot \frac{\Delta p}{p} + \text{h.o. } ... \tag{2.13}$$

The implications of a spread in focusing strength and consequently the tune due to momentum spread Δp will be further interpreted in the next section (2.2.5) of the transversal beam dynamics, where the chromaticity concept will be presented.

2.2.5 Chromaticity

As an analogy to chromatic aberrations in optics, a parameter called chromaticity is used in accelerators. Similarly to the refraction index of a lens, particles with various momentum receive different focusing properties in the quadrupoles and as a consequence have different focal lengths (Fig. 2.12), which again corresponds to a given spread of betatron oscillation frequencies. The idea that the particle beam in the accelerator will have a non-zero momentum spread was introduced in section 2.2.4, with its dependence visible in Eq. 2.13. This suggests that there will be a non-zero betatron tune spread, ΔQ, across the beam, as a result of this relative momentum variation $\frac{\Delta p}{p}$ [14]:

$$\frac{\Delta Q}{Q} \propto \frac{\Delta p}{p} \tag{2.14}$$

This correlation is commonly referred to as chromaticity, and can be written as

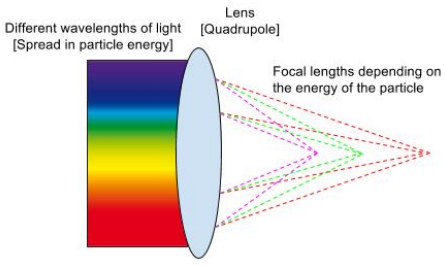

Figure 2.12: Using the focal length of light passing through a focusing lens as an analogy to the difference in a particle's focusing point depending on its energy spread and the setting of the quadrupole it is passing through

$$\frac{\Delta Q}{Q} = \xi \frac{\Delta p}{p} \ , \tag{2.15}$$

where $\xi = Q\prime/Q$, and we can deduce the dependency to its general form

$$\frac{\Delta Q}{Q} = \frac{Q'}{Q}\frac{\Delta p}{p} \Rightarrow Q' = \frac{\Delta Q}{\Delta p/p} \Rightarrow \boxed{Q^{(n)} = \frac{\Delta^{(n)}}{\Delta p/p} Q} \ , \tag{2.16}$$

with n denoting the order of chromaticity. Although there exist higher orders of chromaticity, the signal processing methods in chapter 4 only involve the first order, the so-called *natural chromaticity* Q', which is fundamental for all strong-focusing accelerators, for instance the LHC. We can now combine the tune deviation product from the tune perturbation equation (Eq. 2.13) with the definition of natural chromaticity from Eq. 2.16:

$$Q' = \frac{\Delta Q}{\Delta p/p} = -\Delta Q \frac{1}{4\pi} \oint_C \beta(s) k(s)\, ds \ . \tag{2.17}$$

From the integral, it is clear that the chromaticity depends on the number of quadrupole magnets and their focusing strength ($k(s)$) around the accelerator.

The relative momentum spread $\frac{\Delta p}{p}$ in the LHC is usually in the order 10^{-4}, and the natural chromaticity, usually measured as the quantity $Q\xi$, is in the vicinity of 15 [15]. Inserting these values into Eq. 2.15, the resulting relative tune spread $\frac{\Delta Q}{Q}$ will be in the order of 10^{-2}. Visualizing a tune variation of this magnitude in the tune harmonics diagram in Fig. 2.10, one can deduct that a tune variation of this significance will have a drastic impact on the beams stability.

2.3 Longitudinal beam dynamics

Although the transverse beam diagnostics are in the center for this project, to better understand and calculate the betatron movement, one must be aware of the longitudinal beam dynamics (the accelerating and "bunching" features of the RF). As a vibrating string applies a compressing and decompressing force upon the surrounding air, the RF system is designed to keep the particles inside an enclosed potential energy field, where the particle gain or lose momentum depending on its position. The spatial and temporal topologies of this field define what is called a *bucket*[4] and its dimensions are determined by the applied voltage and its harmonic number.

2.3.1 High energy longitudinal motion

To better understand the principles of the accelerating and bunching properties of the RF field we have to establish how the particle's orbit, speed and momentum change the revolution frequency and how relativity influences this relationship. If we have a constant dipole magnetic field we can write the correlation between the three as $\Delta f_{rev}/f_{rev} = \Delta v/v - \Delta r/r$, where $\Delta f_{rev}/f_{rev}$ is a relative change in revolution frequency, $\Delta v/v$ a relative change in velocity and $\Delta r/r$ a relative change in orbital radius (exactly the same as a relative change in orbit length $\Delta L/L$). If the momentum of the particle increases, the particle moves faster, but as a consequence, the particle will have a longer orbit. This relationship between average orbit and momentum defines the machine dependent parameter momentum compaction factor α_c:

$$\frac{\Delta r}{r} = \frac{\Delta L}{L} = \alpha_c \frac{\Delta p}{p} \ .$$

Using the concluding equation from the first page of chapter 6 in [10]:

$$\frac{\Delta f}{f} = \left(\frac{1}{\gamma^2} - \alpha_c\right)\frac{\Delta p}{p} \ , \tag{2.18}$$

where the momentum compaction factor α_c is a fixed quantity defined by the layout and strength of the magnetic lattice and γ changes as the particle speed changes. Using the momentum compaction factor, Eq. 2.1 in section 2.1.2 and Eq. 2.18 to clarify the relationship between frequency and momentum:

[4] state-space particle acceptance region.

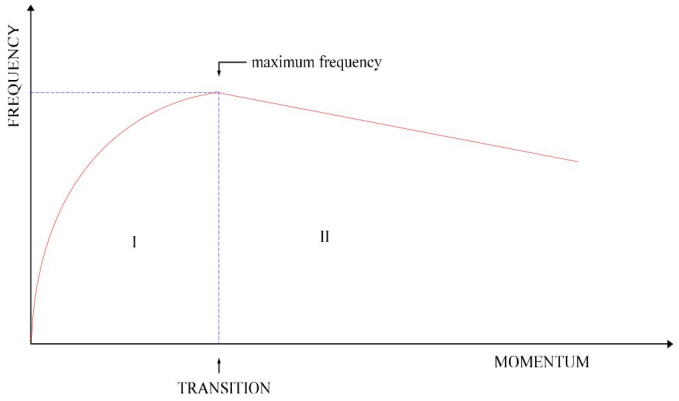

Figure 2.13: Revolution frequency as a function of increase in momentum

- At low energy

$$\beta << 1,\ \gamma \Rightarrow 1,\ \frac{1}{\gamma^2} > \alpha_c \Rightarrow \text{revolution frequency increases as momentum increases}$$

- At high energy

$$\beta \approx 1,\ \gamma \Rightarrow \text{large number},\ \frac{1}{\gamma^2} < \alpha_c \Rightarrow \text{revolution frequency decreases as momentum increases}$$

Note that β, in this case, is not the beta function that describes the betatron motion, but the ratio between velocity and the speed of light from Eq. 2.2. This relation between particle momentum and frequency is illustrated in Fig. 2.13, where the tipping point is given by a transition of maximum frequency. At this transition $\beta \approx 1$ which implies that the particle's velocity is very close to the speed of light and $\frac{1}{\gamma^2} = \frac{1}{\gamma_{tr}^2} = \alpha_c$ ($\frac{1}{\gamma_{tr}^2}$ represents a fixed transition value) as the revolution frequency reaches a maximum value. In region I of Fig. 2.13, $\beta << 1$ and increases rapidly with momentum (from Fig. 2.2 in section 2.1.2) leading to a fast increase in revolution frequency. In region II, i.e. after the transition, $\beta \approx 1$ and the particle velocity is essentially constant while the revolution frequency decreases as a result of the increase in beam momentum hence longer orbit. For accelerating ions in CERN's accelerator chain, this transition occurs in the Proton Synchrotron (PS) at around 6 GeV/c.

To make things simpler we will introduce a relationship between revolution frequency and momentum (from Eq. 2.18) in a accelerator with a parameter called the phase slip factor η:

$$\frac{\Delta f}{f} = \frac{1}{\eta}\frac{\Delta p}{p} \tag{2.19}$$

This parameter will from here on represent the relationship between revolution frequency and momentum in the accelerator, but note that η is both lattice (from α_c) and momentum (from γ) dependent.

The presently available method used to measure the chromaticity in the LHC utilizes relation 2.15. The RF frequency is modulated (more about the RF system in section 2.3.3), hence the beam momentum is modulated, thus the betatron tune spread is also modulated. As the modulation takes place, the tune is being measured simultaneously hence the chromaticity can be calculated. This is an invasive method which, at high beam intensities can cause significant particle losses.

2.3.2 Acceleration

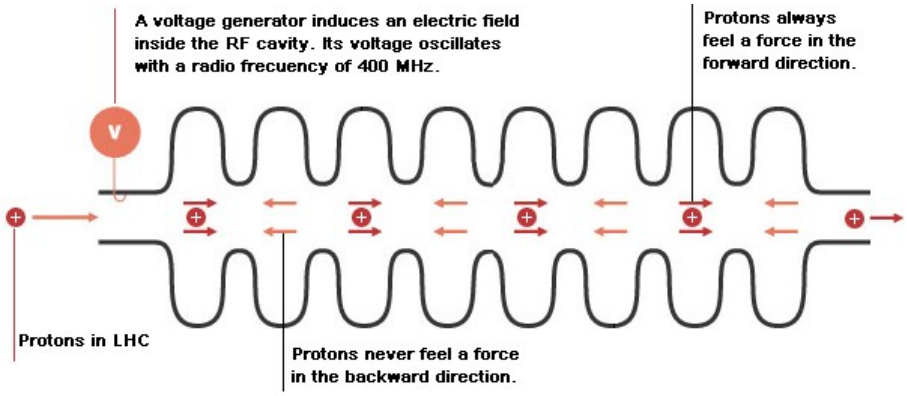

Figure 2.14: Loose illustration of the RF cavities

In order to accelerate the particles, a net force parallel to the particle velocities is required. Lorentz's force is given by

$$\vec{F} = e(\vec{E} + \vec{v} \times \vec{B}). \tag{2.20}$$

From this equation one can immediately see that the net force due to a magnetic field is always perpendicular to the velocity (cross product). This means that only an electric field oriented along the particle's direction of motion can be used to accelerate the beam. The magnetic field (dipole) is used to bend the particle trajectory in order to keep the beam confined in the accelerator. Eq. 2.20 combines the accelerating electric field E with the deflecting magnetic force of the dipoles B to describe the forces acting on a particle with electric charge e traveling at the speed of light c.

2.3.3 RF system

The RF system provides the particles with an accelerating force and keeps them tightly bunched to ensure high luminosity at the collision points. The RF cavities are metallic chambers containing an electromagnetic field. If you imagine beads on a string, the cavities are the beads and the beam pipe the string, loosely illustrated in figure 2.14. The cavities are perfectly molded to build up resonant electromagnetic fields. The electromagnetic waves are supplied by a RF power generator. The charged particles passing through the cavity experiences the force due to this field and gains/loses energy along the direction of motion.

The electromagnetic field formed in the cavities in the LHC is tuned to oscillate at 400 MHz. There are two different regimes for how the particles react to the voltage in the cavities, above transition and below transition (see Fig. 2.13). We will only consider the *above transition* case as this is the operational regime of the LHC. It is relevant to introduce the concept of synchronous particle, in stationary conditions, as the particle that will always gain as much energy as it loses per turn. In the case of the LHC, operating with protons or ions, radiation losses are negligible hence the synchronous particle is the one that will always see a zero electric field (i.e. zero RF phase) as it passes the cavity. Particles with different energies arriving earlier or later than the synchronous particle will be accelerated or decelerated, while the latter, with exactly the machine's nominal energy and zero phase difference with respect to the RF wave, will not see any accelerating voltage. As explained in Fig. 2.15, this process sorts the particles into discrete bunches.

Because of this bunching effect the particles are not uniformly spread throughout the accelerator, but held together in bunches, which again are contained within so-called RF buckets (Fig. 2.16). The particle gains or loses energy according to the equation

$$\Delta E = eV sin(\delta\phi) \ , \tag{2.21}$$

where ΔE is the energy lost or gained according to the particle's phase deviation $\delta\phi$ with respect to the oscillating RF voltage V. A smaller or larger voltage V or frequency makes the particles follow a more elliptical or circular orbit. This RF bucket can be thought of as a well of potential energy, where the particles will remain trapped and oscillate longitudinally back and forth given

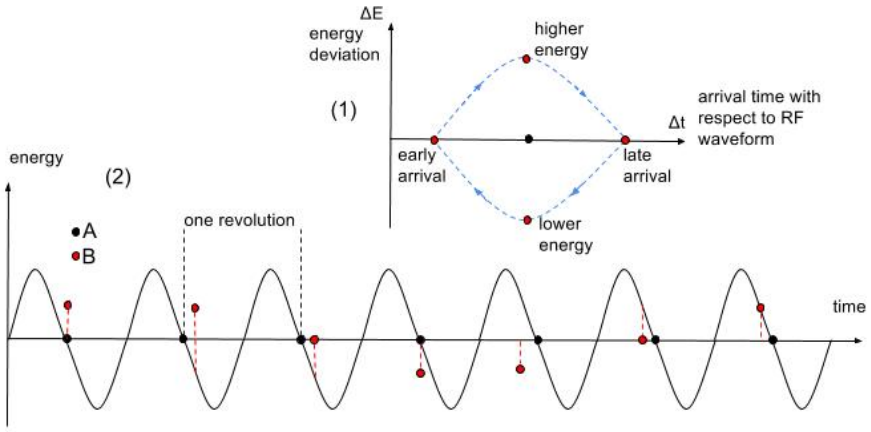

Figure 2.15: Particle A is the synchronous particle, as a consequence, it will not experience any accelerating force. The second particle B arrives at the same time as A but has a slightly higher momentum. When particle B passes the cavity in the following turn it will arrive later than A (assuming we are above transition) and encounter a decelerating voltage. In the third turn, B now has the same momentum as A as a consequence of the decelerating force it received the last turn. Even though they have the same momentum, particle B still arrives later and therefore experiences a deceleration. After a few more turns, the particle will have returned to its original position and the cycle repeats itself. All particles in the accelerator, like particle B, will oscillate longitudinally around the synchronous particle A under the influence of the RF system. This motion is called synchrotron oscillations and is shown in a loosely longitudinal phase space plot (1).

that their energy deviations are less than the depth of the bucket (Fig. 2.16). These longitudinal oscillations are called synchrotron oscillations. Particles inside a bunch perform this oscillatory longitudinal motion periodically at a frequency that is called the synchrotron frequency. In the LHC, the synchrotron frequency is of the order of tens of Hz.

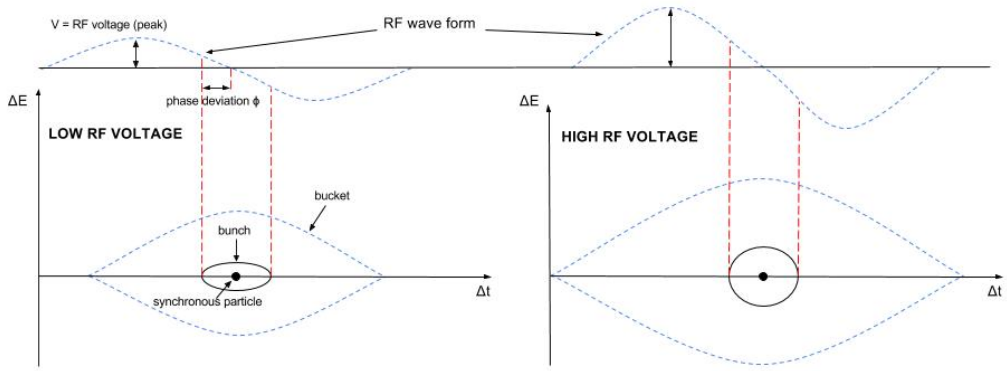

Figure 2.16: Bunch shapes depending on different RF frequencies and voltages

2.4 Brief summary

This chapter was just an introduction to the synchrotron accelerator physics, emphasizing the elements concerning the measurements of the Schottky signals which will be presented in chapter 3. Although this might be a dense read, it is nevertheless an essential preparatory for understanding the next chapters. A small revision of the most relevant details should be in order:

- the storage rings consist of dipole magnets that keeps the particles in a closed circular path, quadrupoles and other higher order magnets that provide a transverse focusing feature, RF cavities to accelerate and sort particles into discrete packets, and drift spaces where there is no change in the momentum of the particle (Fig. 2.17).
- The tune Q is the number of betatron oscillations a particle performs in a revolution of the accelerator, where the fractional part q must be an irrational number to avoid resonance and risk being lost in the accelerator. There are a number of perturbation sources, such as; different magnetic errors; coherence between the planes (the impact of q_h on q_v and vice versa); and other machine imperfections. All of these tune disruptions must be measured and corrected to restore beam stability.
- The relative momentum spread $\frac{\Delta p}{p}$ can also cause a significant spread in tune, and the correlation between the two is known as chromaticity ($\xi = Q'/Q$).
- When working with beam dynamics above the relativistic transition ($\beta \approx 1$ and $\gamma \Rightarrow$large number), the particles enter the regime of special relativity. A further increase of momentum above transition will reduce the revolution frequency and reduce the size or emittance of the beam.

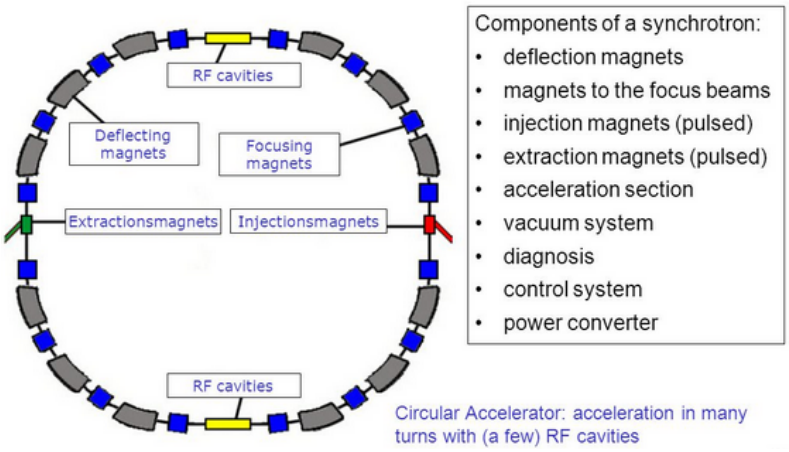

Figure 2.17: Components of a synchrotron accelerator

Chapter 3

Schottky Signals

In this chapter, we will mainly get acquainted with the theoretical background of the signals measured by Schottky systems. The origin of the principles governing Schottky signals in accelerators goes back to the shot noise first observed 100 years ago. As a gradual introduction, we will start with the measurement of a purely longitudinal signal of an unbunched beam, and work our way towards the analysis of both bunched longitudinal and transverse beam signals.

The LHC Schottky beam diagnostics system was designed with the intent of measuring important beam parameters such as tune, chromaticity, synchrotron frequency, momentum spread, etc. As will be shown throughout this chapter, the information on the previously mentioned beam parameters is encoded in frequency spectrum obtained.

3.1 Shot noise

Shotnoise was discovered by the German physicist Walter Schottky in 1918 while he was experimenting with vacuum tube amplifiers. He noticed that the current fluctuations measured on the anode consisted of distinct impulses of charge from the individual electrons arriving at the electrode.

Shotnoise occurs when you have a system in which there are distinct transition effects of charged carriers. A basic example is to think of two plates, a cathode and an anode, in a vacuum connected to a DC voltage supply, just like in a vacuum diode (Fig. 3.1). In this vacuum there will be electrons moving from the cathode to the anode. An electron will either be accelerated or not to the other side. Like in a PN-junction, where you either have electrons going to the other side or not, an exchange of half an electron is not possible. Another example would be a photosensor, where the photons are picked up as discrete packets of energy, you cannot have half a photon arriving at the anode. In other words, the current is in reality formed by these very distinct transition events or impulses of charge as illustrated in Fig. 3.2. What Schottky noticed during his experiments was that with sufficient gain, he could identify these impulses within the signal (upper plot in Fig. 3.2). After sufficient amplification, he could hear the crackling of the electrons moving from the anode to the cathode and hence named it shot noise. Intuitively a short-circuited current (a direct current) generates a total shot noise Power Spectral Density (PSD) $S_i(\omega)$ given by:

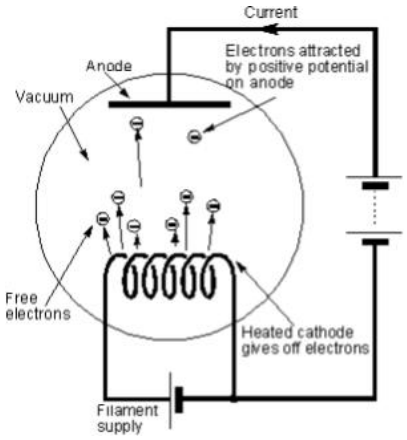

Figure 3.1: Vacuum diode

$$S_i(\omega) = \frac{d\langle i^2_{shot}\rangle}{df} = 2eI_0 \ , \tag{3.1}$$

where e is the elementary charge, the angled brackets denote the inner product over many events of the stochastic emittance of electrons, and I_0 the DC (direct current). Applying a Fourier transform to the signal produces a double-sided spectrum that is mirrored around the DC current.

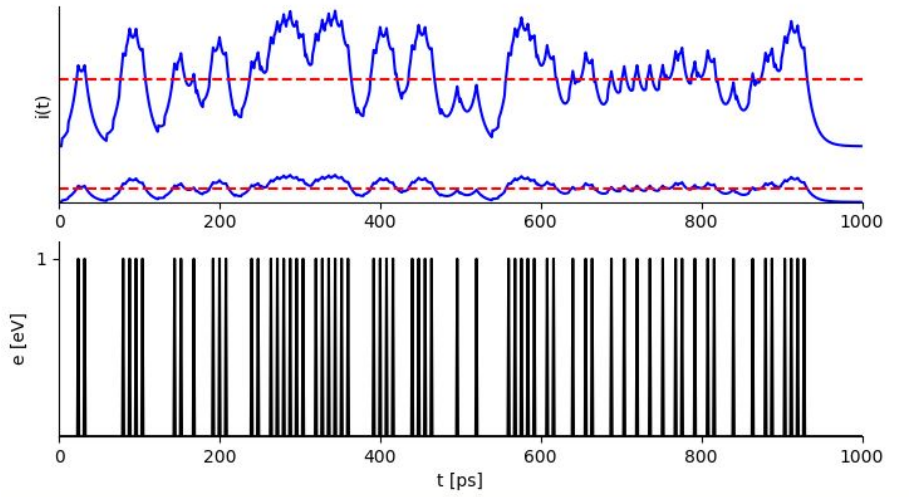

Figure 3.2: Bottom frame is the stochastic emittance of electrons, while the upper is the corresponding current produced. The different current levels is to display the significance of increased gain to more easily distinguish the shot noise(blue) from the mean current(red line)

Converting this to a single-sided spectrum result in a doubling of the power at each frequency. For some additional information on Schottky's experiments with vacuum tubes and the resulting PSD, or the comparison between thermal noise and shotnoise check out the paper about Schottky signals [1].

3.2 Schottky signals

Depending on the analog signal processing employed, a Schottky system can be optimized for probing either the longitudinal or transverse particle dynamics. Furthermore, the acquired signals themselves exhibit different characteristics depending on whether the beam is bunched (i.e. RF present) or unbunched. Beam parameters such as betatron tune, chromaticity and synchrotron frequency are best suited to be calculated in the frequency domain as we will see below.

3.2.1 Unbunched beam / longitudinal plane

Consider a single particle with revolution frequency f_{rev}; the measured current will be given by an infinite train of delta pulses m, separated by the nominal revolution period T_{rev} (Fig. 3.3):

$$i(t) = \frac{e}{T_{rev}} \sum_{m-\infty}^{\infty} \delta(t - mT_{rev}) = i_0 \sum_{m-\infty}^{\infty} \delta(t - mT_{rev}) \ . \tag{3.2}$$

The Direct Current (DC) i_0 is given by the number of times the particle passes the pick-up system in a second $i_0 = ef_{rev}$. In the frequency domain however, the periodic waveform is shown as a line spectrum (fig 3.4), where the distance between the lines is f_{rev} separated at discrete harmonic numbers n. Applying a Fourier analysis to the train of delta pulses in equation 3.2 over all harmonic

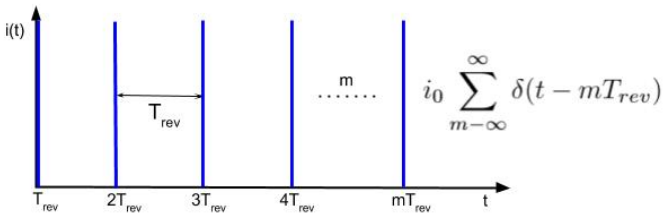

Figure 3.3: Single particle circulating the accelerator at a period of T_{rev}

frequencies nf_{rev} gives us

$$i_i(t) = i_0 + 2i_0 \sum_{n=1}^{\infty} a \cdot cos(n2\pi f_{rev} t) + a \cdot sin(n\pi f_{rev} t) \begin{cases} i_0 = e f_{rev} = \text{DC current} \\ a_n = cos(n\phi_0) \text{ and } b_n = sin(n\phi_0) \end{cases} . \quad (3.3)$$

Since we are not interested in the negative frequencies, we will convert the equation to represent a single-sided spectrum where the cosines term of the Fourier sequence will represent the line spectrum of a particle with frequency f_i:

$$i_i(t) = i_0 + 2i_0 \sum_{n=1}^{\infty} a \cdot cos(n2\pi f_i t) \ . \quad (3.4)$$

Fig. 3.4A shows the positive harmonic frequencies separated by the harmonic number n.

If we now were to add a second particle to circulate the accelerator, at a slightly different frequency, the frequency of this second particle would be given by:

$$f_1 = n \cdot (f_0 + \Delta f) = nf_0 + nf_0 \cdot \eta \frac{\Delta p}{p} \ . \quad (3.5)$$

Here the f_0 is supposed to be the synchronous particle circulating at f_{rev}, and f_i a particle with a different frequency as a consequence of a relative momentum spread that depends on the phase slip factor η (introduced in Eq. 2.19). This would introduce another line in the frequency domain separated from the synchronous particle by the frequency offset Δf multiplied by the harmonic number n (Fig. 3.4 B).

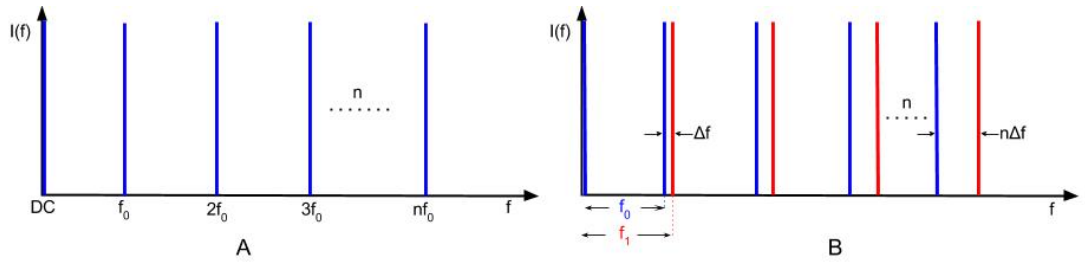

Figure 3.4: A shows the frequency spectrum of a single particle circulating the accelerator. In B there is an additional particle with a relative momentum spread, which causes it to have a different revolution frequency.

Now we add a large number of particles N to the unbunched beam circulating the the accelerator, each with a distinct frequency (infinitely narrow pulse width in the frequency domain). These particles will now replace the separate lines with a band containing all the particle's frequencies. The width of this band will be $n\Delta f$ (established in Eq. 3.5), except now f_0 will denote the average revolution frequency as we have both negative and positive deviance (Fig. 3.5). A thing to note is that both f_0 and f_{rev} represents the same thing, but f_0 is the average and most

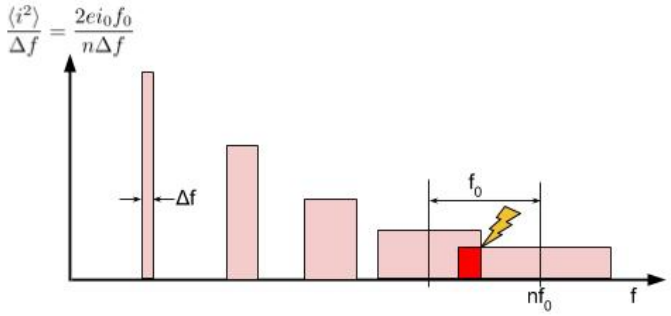

Figure 3.5: Power spectral density of the longitudinal Schottky signal (f_0 is the revolution frequency in this case) where the height of the spectral density reduces as the harmonic number n increases, which causes the width of the band to increase since the spectral density remains the same.

likely synchronous particle, while f_{rev} is the actual ideal particle. If we now average equation 3.4 over N particles with different frequencies F_I, only the DC component $i_0 = Nef_{rev}$ will remain. The total power of the signal however, gives us a squared current of [16]:

$$\langle i_i^2 \rangle = \left\langle \left(2ef_{rev}\right)\left[\sum_N cos(n2\pi f_i t)\right]^2 \right\rangle = \left(2ef_{rev}\right)^2 \sum_N \left\langle cos^2(n2\pi f_i t)\right\rangle = 4ef_{rev}^2 N\frac{1}{2} = 2ef_{rev}^2 N \tag{3.6}$$

We can now also calculate the Root-Mean-Square (r.m.s.) current per band:

$$i_{rms} = \langle\sqrt{i^2}\rangle = 2ef_{rev}\sqrt{\frac{N}{2}}\ . \tag{3.7}$$

The power and r.m.s. current per band (Schottky current) is now independent of the harmonic number n, so the total area in the spectrum must stay the same. From Eq. 3.5 however, we know that the width of the band increases with the harmonic number. Since the total signal power from the particles is the same, the amplitude of the sideband must decrease to preserve the same area. An implication of this is that with the increase of frequency spread the sidebands will eventually overlap, leading to corrupted spectra due to their interference with each other (Fig. 3.5) [1].

3.2.2 Unbunched beams / transverse

We will again start with a single particle, but this time it performs betatron oscillations. At a Schottky pick-up, this particle will produce a train of impulse functions modulated by the betatron oscillations. The measured current for this single particle is described by the dipole moment $d(t) = a_i(t) \cdot i_i(t)$, where $a_i(t)$ is the transverse displacement and $i_i(t)$ is due to the longitudinal motion. The i_{th} particle executes a sinusoidal betatron oscillations of amplitude a_i, which can be written as:

$$a_i(t) = a_0 + a_i cos(q\omega_{rev}t + \phi_i)\ , \tag{3.8}$$

where a_0 is the average transversal displacement in the accelerator, a_i is the amplitude of the betatron oscillation, $q\omega_{rev}$ is the betatron frequency, and ϕ_i the initial betatron phase. Fig. 3.6 portrays the measured impulses due to the periodic passing of the particle in front of the pick-up modulated by the transverse betatron oscillation.

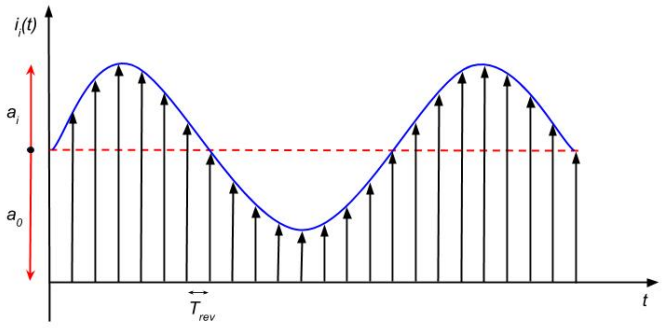

Figure 3.6: Time domain representation of a single particle's betatron oscillations. Each line spread by the revolution period T_{rev} is the pulses the pick-up measures, and thereafter modulates a sinusoidal signal. In the LHC the particles normally executes 50-70 betatron oscillations in one revolution [5], this plot is just to get an idea of how the modulation occurs.

In general, if the beam is displaced (on average) from the centre of the Schottky pick-up, the Schottky system can be sensitive to both the transverse (Eq. 3.8) and longitudinal (Eq. 3.4)

particle motion. The signal in the time domain can be written as:

$$d_i(t) = \Big[a_0 + a_i cos(q\omega_{rev}t)\Big]\Big[ef_{rev} + 2ef_{rev}\sum_{n=1}^{\infty} cos(n\omega_{rev}t)\Big] \ , \ (ef_{rev} = i_0)$$

$$= a_0 ef_{rev} + a_0 2ef_{rev}\sum_{n=1}^{\infty} cos(n\omega_{rev}t) + \tag{3.9}$$

$$a_i ef_{rev}\Big[cos(q\omega_{rev}t) + \sum_{n=0}^{\infty} cos(n-q)\omega_{rev}t + \sum_{n=1}^{\infty} cos\big((n+q)\omega_{rev}t\big)\Big]$$

In the previous equation, one can recognize that it has an average transverse displacement (1st term), a longitudinal part due to its revolution frequency (2nd term) and a transverse part that has both a positive and negative betatron frequency qf_{rev} (3rd term). What we get is a Amplitude Modulated (AM) signal, which implies that we will have a center frequency given by the carrier f_{rev} (2nd component) and two mirror-imaged sidebands at each side ($\pm qf_{rev}$).

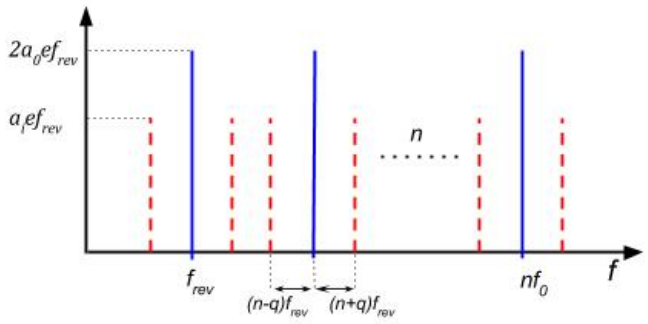

Figure 3.7: Frequency spectrum of a single particle performing both betatron and longitudinal oscillations

Average the from Eq. 3.9 for a given harmonic number n, tune q and a large number of particles N would give:

$$\langle d_i \rangle = 0 \quad ; \quad \langle d_i^2 \rangle = \langle a_i^2 \rangle e^2 f_0^2 \frac{N}{2} \tag{3.10}$$

$$d_{rms} = ef_0 a_{rms}\sqrt{\frac{N}{2}} \tag{3.11}$$

Again the total power per Schottky band $\langle d^2 \rangle$ is independent of the harmonic number n and proportional to the number of particles in the beam, but this time it is also proportional to the square of the average betatron amplitude $\langle a_i^2 \rangle$.

Each Schottky band has now a finite width which results from the spread of revolution frequencies $\Delta f = f_{rev}\eta\Delta p/p$ (from Eq. 2.18) and from the spread of betatron frequencies due to tune q. The latter usually comes from the machine chromaticity $\Delta q = Q\xi\Delta p/p$ (from Eq. 2.15). If we now add these changes in betatron frequency to the transverse part of (3rd component) of Eq. 3.9, the width of two adjacent Schottky bands $(n \pm q)$ will be given by:

$$\Delta f = (n \pm q)f_{rev} \pm 2\pi f_{rev}\Delta q_i$$

$$\Delta f_{lsb,usb} = f_{rev}\frac{\Delta p}{p}\big[(n \pm q)\eta \pm Q\xi\big] \ , \tag{3.12}$$

if only chromaticity contributes to the betatron frequency spread.

Since the harmonic number n and betatron tune q is the same for all the particles, the size of the betatron sidebands from Eq. 3.12 change according to the chromaticity. Positive chromaticity increases the width of the sideband, while negative chromaticity makes the sideband narrower. Typically the lower sideband has positive chromaticity and the upper sideband negative.

For this paper we are more interested in the bunched particle beams considering this is how the particles are received in the LHC from the SPS. Although the randomness declines under bunched conditions due to coherent properties (particles affect each other and collectively feel the same perturbation effects) it is still possible to measure the noise-like signals as before.

3.2.3 Longitudinal Schottky signals of bunched beams

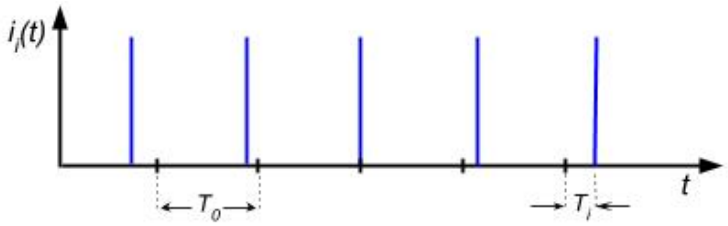

Figure 3.8: Measured pulses from a single particle in a bunched beam in the time domain. The modulated time arrival is due to its synchrotron oscillation (check out figure 2.15 in section 2.3.3).

Once again we return to the premise of having a single particle in the accelerator, but this time with an operational RF system, which means the particles will be sorted into discrete bunches (section 2.3.3 RF). When particles are bunched, they execute synchrotron oscillations with a synchrotron frequency f_s. This means that the particles no longer oscillate inside the accelerator at $T = T_{rev}$, but is modulated in time as

$$\tau_i(t) = \hat{\tau}_i sin(\Omega_s t + \psi_i) \ , \tag{3.13}$$

where $\tau_i(t)$ is the modulation in time with respect to he synchronous particle T_{rev}, $\hat{\tau}_i$ the synchrotron oscillation amplitude, $\Omega_s = 2\pi f_s$ the synchrotron frequency and ψ_i the initial phase of the particle. In the time domain the beam current is represented as a series of delta pulses (Fig. 3.8), with a modulated time of passage that can be written as:

$$i_i(t) = ef_0 + 2ef_0 Re\left\{ \sum_{n=1}^{\infty} e^{jn\omega_{rev}\left[t+\hat{\tau}_i sin(\Omega_s t+\psi_i)\right]} \right\} . \tag{3.14}$$

Here the cosine term (from Eq. 3.4) is replaced with an exponential notation, still only considering the real values Re. Using the notion that the harmonic distribution of a phase modulated signal can be represented as Bessel lines (check out Eq. 66 in [17]):

$$e^{j(xsin(\theta))} = \sum_{p=-\infty}^{\infty} J_p(x) e^{jp\theta} \ , \tag{3.15}$$

where J_p is the Bessel function (of the first kind) of the order p. This means we can expand the amplitude of the n^{th} harmonic component in equation 3.14 using the Bessel function notion:

$$i_n = 2ef_{rev} Re\left\{ \sum_{p=-\infty}^{\infty} J_p(n\omega_{rev}\hat{\tau}_i) e^{h(n\omega_{rev}t+p\Omega_s t+p\psi_i)} \right\} . \tag{3.16}$$

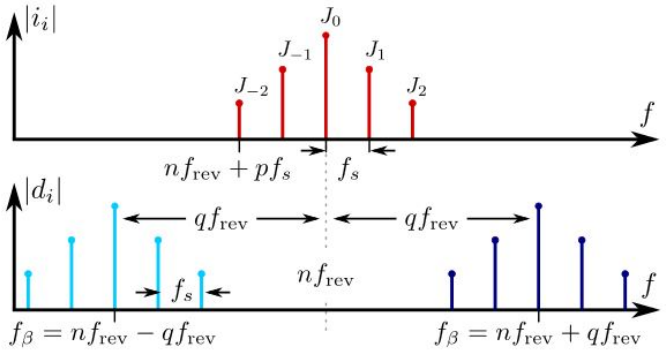

Figure 3.9: Longitudinal i_i and transverse d_i bunched Schottky signals for a single particle executing synchrotron oscillations

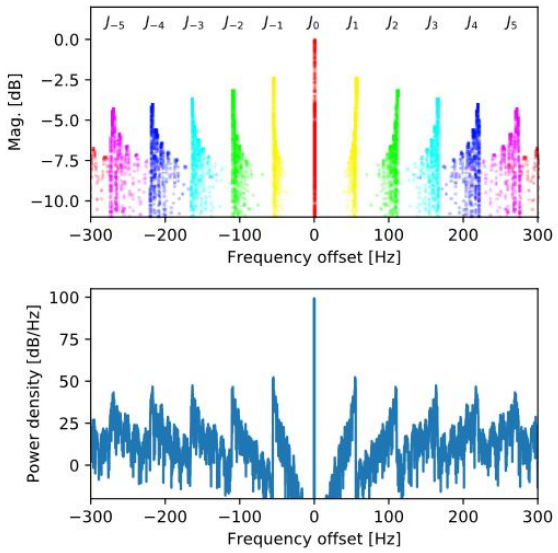

Figure 3.10: Upper plot: Monte Carlo simulation of a longitudinal Schottky spectrum at 4.809 GHz, visualizing Eq. (4) for 10^6 simulated particles with parameters typical for the LHC at injection energy. The points represent phasor magnitudes and have been color coded according to the order of the Bessel function p. Lower plot: Simulation of a spectrum analyzer measurement by using a sliding window for binning and vector-summing the points within a resolution bandwidth of 1 Hz [19].

This gives us the full definition for the longitudinal signal for a particle in a bunched beam:

$$i_i(t) = ef_{rev} + 2ef_{rev}Re\left\{\sum_{n=1}^{\infty}\sum_{p=-\infty}^{\infty} J_p(n\omega_{rev}\hat{\tau}_i)e^{h(n\omega_{rev}t+p\Omega_s t+p\psi_i)}\right\}. \tag{3.17}$$

This means that the revolution frequency for the particle in the frequency domain now splits into an infinite number of synchrotron satellites spaced by the synchrotron frequency f_s. The amplitude of each satellite is proportional to the order of the Bessel function of the argument $n\omega_s\hat{\tau}_i$ and is symmetrical around nf_{rev} due to 180 phase shifts for negative values of p as illustrated in red in Fig. 3.9 [1; 16; 18].

From now on we will start to narrow down the general theoretical background of the Schottky signals, to focus more on the LHC Schottky pickups by including real examples and simulations from the measurement system. There will be a great deal of referencing to other papers and articles, but the most important concepts will be present.

Again, adding a large number of particles N, but we also include the synchrotron oscillations. We will then see synchrotron satellites inside the 'significant bandwidth' for each particle [19]. These synchrotron satellites will be randomly distributed around the synchrotron lines from Fig. 3.9. In the upper plot of Fig 3.10 this has been simulated for $N = 10^6$ particles in the frequency domain using Eq. 3.17, where each dot corresponds to a certain amplitude, frequency and initial phase and color-coded accordingly to represent a synchrotron satellite with index p [19]. In Fig 3.10 the center frequency (0) represents the harmonic number of the LHC Schottky system $n = 427727$, which is the revolution harmonic $nf_{rev} = 4.809$ GHz. More about the operational frequency and the analog signal chain in section 4.1.

In the center line $p = 0$, all points fall on the same place since the synchrotron frequency Ω_i and initial phase ψ_i from Eq. 3.17 is zero, which results in a strong, coherent peak. Except for the center line, the power of the synchrotron satellites adds up non-coherently due to their random phase ψ_i and frequency f_s. This non-linear relationship gives rise to spread in synchrotron frequency Δf_s, which turns the synchrotron satellites for $p > 0$ into frequency bands of width p_s. Due to different machine perturbations, like fluctuations in the magnetic field or RF, we get a spread in the revolution frequency Δf_{rev} that again broadens the spectral features even further. This makes the structure in the longitudinal Schottky spectrum disappear for large numbers of n or p, when bands are overlapping at $p\Delta f_s > f_s$ and $n\Delta f_{rev} > f_s$.

In practice, the width of the central line will not be infinitely thin because of imperfections

in the RF and magnetic dipole field. Have a look at Fig. 4.7 in the next chapter for a real portrayal of the longitudinal synchrotron lines around the Schottky harmonic.

3.2.4 Transverse Schottky signals of bunched beams

To get the transverse Schottky signals of a bunched beam, we again (as with Eq. 3.9) have to combine the AM signal due to betatron motion (Eq. 3.8 and the now phase modulated synchrotron motion (Eq. 3.14):

$$d_i(t) = \left[a_0 + a_i cos(q\omega_{rev}t)\right]\left[ef_{rev} + 2ef_{rev}Re\left\{\sum_{n=1}^{\infty} e^{jn\omega_{rev}\left[t+\hat{\tau}sin(\Omega_s t+\psi_i)\right]}\right\}\right] \tag{3.18}$$

As for the unbunched transverse signal case (section 3.2.2), the amplitude modulation for one particle will split each line into two betatron lines at frequencies $(n-q)f_{rev}$ and $(n+q)f_{rev}$). The phase modulation will then further subdivide this center line into satellites spaced by the synchrotron frequency f_s. This is illustrated in the bottom plot in Fig. 3.9, where the teal lines represent the negative tune and the purple lines positive tune [18].

Assuming the beam is centered in the accelerator (a_0=0) when it passes the Schottky monitor we can isolate the betatron oscillations giving us the synchrotron line for a single particle:

$$d_i(t) = ef_{rev}a_i Re\left\{\sum_{p=-\infty}^{\infty} J_p\left[(n\pm q)\omega_{rev}\hat{\tau}_i\right]e^{j\left[(n\pm q)\omega_{rev}+p\Omega_s t+p\psi_i+\phi_i\right]}\right\} \tag{3.19}$$

For a large number of particles N, the signal will be averaged for different initial betatron (ϕ_i) and synchrotron (ψ_i) phases, turning the lines shown for a single particle in figure 3.9 into bands in a similar way as for the longitudinal case (Fig. 3.10). It is important to note that due to the random initial betatron phase, the center line ($p = 0$) does not add as coherently as in the longitudinal case, leading to a significant difference between the peak power at the coherent longitudinal and betatron center frequencies (Fig. 3.11). As mentioned in section 3.2.2, the width of the betatron sidebands are dominated by the spread of revolution frequency Δf_{rev} and tune Δq_i. In high energy machines like the LHC, the latter is more significant and mainly originates from a non-zero chromaticity.

It is important to note that equation 3.19 only considers the incoherent transverse Schottky signals of the bunched beam, i.e. the particles only follow unperturbed synchrotron and betatron motion. In reality the particles in the LHC and other hadron ring accelerators suffer from multiple sources of coherent forces that makes makes the particles act as a semi-rigid body, e.g. from instabilities (head-tail, electron-cloud), impedance effects, driven kicks, (RF modulation, dipole kicks) etc.. These coherent effects can lead to several peaks with coherent tunes that is not necessarily centered at the transverse sidebands. Check out [18; 19] for more non-linear or higher-order effects.

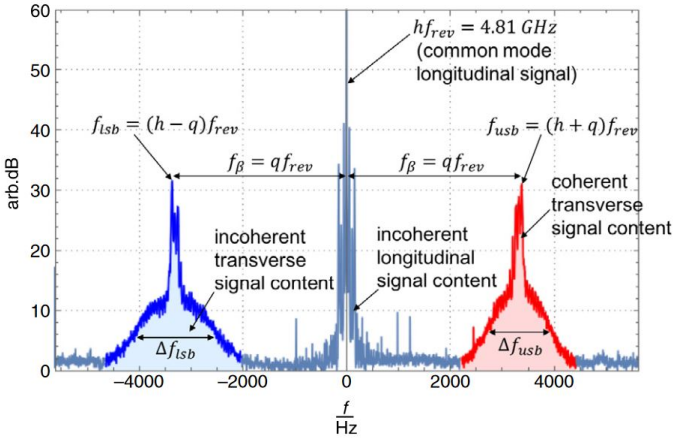

Figure 3.11: Example of the LHC Schottky spectrum at injection energy [1].

For a non-zero chromaticity ($Q' = Q\xi \neq 0$) the Bessel function in Eq. 3.19 must be changed to:

$$J_p\Big[\big((n \pm q) \pm \frac{Q\xi}{\eta}\big)\omega_{rev}\hat{\tau}_i\Big] \ , \tag{3.20}$$

$\frac{Q\xi}{\eta}\omega_{rev}$ being the *chromatic frequency*. As already stated, this non-zero chromaticity is positive for the lower sideband and negative for the upper sideband. This causes an asymmetry in the widths of the sidebands where the lower sideband is wider than the upper (Fig. 3.11). For large harmonic numbers this width is significant enough to be used to calculate the chromaticity from evaluating their widths:

$$Q' = Q\xi = \eta\left(n\frac{\Delta f_{lsb} - \Delta f_{usb}}{\Delta f_{lsb} + \Delta f_{usb}} + q\right) \tag{3.21}$$

In section 4.2, algorithms for extracting the the widths of the lower (Δf_{lsb}) and upper (Δf_{usb}) sidebands will be presented. Once the widths are established, equation 3.21 is used to determine the chromaticity.

Chapter 4

Signal processing

4.1 Analog signal treatment chain

The analog treatment chain has two separate parts, front-end and back-end. The former is associated with 'front-end' because is the signal processing stage from the electromagnetic receivers and up to the mixers, and is mounted directly on top of the Schottky beam pickups. The back-end consists of frequency down-mixing stages for converting the frequency from a microwave to audible spectrum and then digitizing the signal. It is located in a nearby alcove that is isolated from the LHC tunnel.

4.1.1 the beam pickups

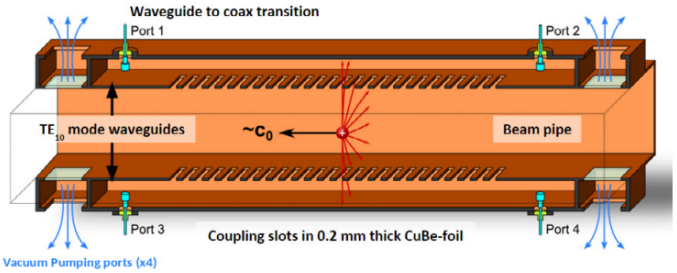

Figure 4.1: Cross section of the LHC Schottky pickup seen from the side. The pickups are designed to direct the electromagnetic waves emitted from the charged beam via two slotted waveguide systems (one on each side in its designated plane) to the coaxial pickups. The four vacuum pump ports are there to make the device uphold LHC vacuum requirements.

The Schottky beam pickups (Fig. 4.1) are mainly designed to be sensitive to the transverse fluctuations of the bunches. They are designed to couple to the beam at 4.8 GHz, which corresponds to the harmonic number $n = 427727$ ($nf_{rev} \approx 4.8$), with a bandwidth of 200 MHz. This specific operation frequency is chosen as an optimal working point considering the trade-off between strong coherent signals at lower frequencies and overlapping Schottky sidebands at higher. Figure 3.5 in section 3.2.1 illustrates how the power spectral density at higher frequencies bleeds into the adjacent spectrum while suffering from strong coherent signals at lower frequencies. There are in all 4 Schottky pickups in the LHC, one for each beam and both planes.

4.1.2 Front-end

The first part of the treatment chain is mounted directly on top of the pickups and provides common mode rejection, gating for processing the signal of preferred bunches, filtering and amplification (Fig. 4.2).

First step of the front end chain is a hybrid that differentiates the signal from each side of the beam to suppress the unwanted common mode signals. One of the lines is equipped with a fixed

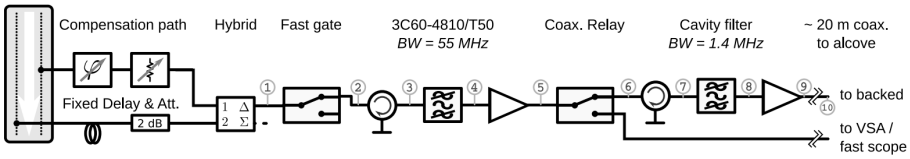

Figure 4.2: Block diagram of the front-end electronics that are mounted directly on top of the beam pickups

attenuator and delay line, while the other is motorized for the possibility of adjustments. After the compensation path, the signal continues to a fast gating circuit, which provides possibility to "listen" to specific bunches while minimizing the influence of beam pipe reflections. Reflections causes a unwanted ringing effect that remains after a beam has passed through the pick-ups, which may results in the active components more easily reaching saturation and thus distorting the wanted signal.

The design of the microwave electronics is a trade-off between reduced distortion and higher sensitivity. For increased sensitivity, the weak transverse Schottky sidebands must be amplified to surpass the inherent thermal noise of the microwave components along the chain. Furthermore, because of the strong coherent signal surge from the passing beam, the gain must be distributed carefully along the chain to keep further unavoidable distortion to a minimum. Too much distortion can lead to an elevated noise floor, which can overshadow the weak transverse Schottky sidebands. To keep it short, the notable remains of the front-end electronics consist of two bandpass filters and two amplifiers. The first bandpass filter contributes with a wide 55 MHz bandwidth that provides frequency pre-selection and prevents excessive peak power at the input of the following amplifier (5), which has a modest gain of G=12dB but high linearity and low noise figure. This amplification step functions as compensation for the resulting losses of the subsequent filter (8), which has a relatively narrow bandwidth of 1.4 MHz that reduces the peak power during the bunch passage for all successive components. The last component in the front-end part of the treatment chain is a amplifier (9) that provides a high gain of G=45dB to minimize the effect of future noise and compensate for the transmission losses the signal will experience from the tunnel to the alcove where the back-end electronics are located.

4.1.3 Back-end

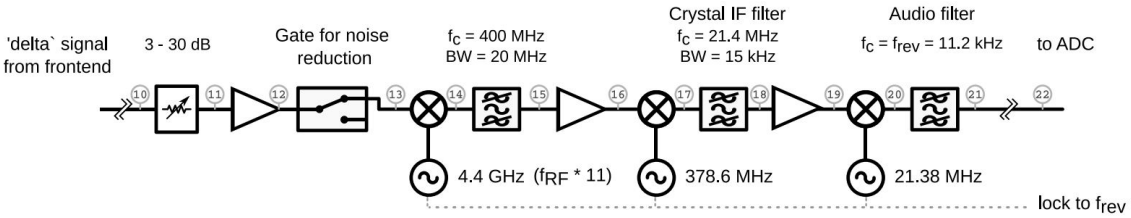

Figure 4.3: Block diagram of the back-end components located in a alcove alongside the LHC tunnel. The main purpose of this stage of the analog treatment chain is to down convert and digitize the signal.

The back-end part of the treatment chain is located in a alcove alongside the tunnel, connected to the front-end with a 20m long coaxial connection ((Fig. 4.2 (10)). The first of the back-end electrical equipment is a variable attenuator (11) that adjusts the incoming signal level. The next significant component is a gate (13) that substantially improves the signal to noise. Since the Schottky signal has a very low duty cycle (the signal is present at short intervals, i.e. much lower off-time than on) and the thermal noise induced by the active components at any stage of the analog treatment chain is always there, the gate (13) is crucial.

The signal is then down-converted through a cascade of 3 frequency mixer stages to an audible frequency. The first mixer (14) is driven by a local oscillator which is harmonically derived from the accelerators RF frequency with a frequency multiplier ($f_{RF} \cdot 11 = 400\ \text{MHz} \cdot 11 \approx 4.4$ GHz). This intermediate frequency ($f = (4.8 - 4.4)\ \text{GHz} = 400\ \text{MHz}$) is then passed through a bandpass filter of 20 MHz (15) which is then again down-converted to 21.4 MHz (17) since this is

the standard frequency for the following narrow-band crystal filters (18,21). After the last down-conversion and filtering stage (20,21), the signal is digitized with a 24-bit digitizer at a sample-rate of $4f_{rev}$. As shown in Fig 4.2 both the local oscillators and the Analog-to-Digital Converter (ADC) clock at the end of the chain are locked to f_{rev} to ensure that there will not be any frequency drifts in the resulting spectra, even during energy ramp when the RF frequency changes.

4.2 Digital signal processing

A typically acquired spectrum spans from $-f_{rev}$ to f_{rev} and is centered around the harmonic frequency of the Schottky system ($nf_{rev} \approx 4.8GHz$). The Graphical User Interfaces (GUIs) or other figures shown in this report might range from $-f_{rev}$ to f_{rev} (Fig. 4.4) or as a frequency normalized to f_{rev} (from -1 to 1) (as in Fig. 4.6). This implies that there should be 3 revolution harmonics visible at -1, 0, and 1, but only the middle one (0) is visible due to the crystal IF filters bandwidth of 15 kHz. Since the ADC clock is fixed at $4f_{rev}$, the revolution frequencies will stay in these fixed positions in the spectrum. Furthermore, there are four sidebands visible in an acquired spectrum; this is because each harmonic frequency has betatron sidebands. The two sidebands in the center are associated with the center revolution (0) harmonic, the left sideband to the -1 revolution harmonic, and the right sideband to the +1 revolution harmonic.

Until now we have made clear what the possibilities are for extracting important beam parameters from the internal statistical fluctuations of the particles, i.e. the Schottky noise. The methods that have been developed for measuring tune and chromaticity is built to be robust and operational for both injection (650 GeV) and collision energy (6.5 TeV). The reason for this is that the transverse sidebands change significantly when the beam is accelerated from injection to collision energy. The total power of the sidebands is linked to the emittance (beam size) of the beam, which again is proportional to the relativistic gamma of the beam [10]. The concept of reduced emittance ϵ due to increasing energies above the relativistic transition was introduced in section 2.2.3. This is apparent in Fig. 4.4, as the measured betatron frequencies that makes up the size of the sideband, experiences a total power loss of 7 dB when the beam is accelerated from injection to collision energy.

In addition to the measurement of tune and chromaticity, there has been developed a method to estimate the synchrotron frequency by applying a Discrete Fourier transform (DFT) on a portion of the spectra with strong synchrotron lines to capture their periodicity.

It is also important to note that there are 4 pickups for the Schottky system, one for each combination of plane and beam, e.g. one spectrum for beam 1 in the horizontal plane, beam 2 in the vertical plane, etc. All the methods are the same for each acquired spectrum (the combination of beam 1 or 2, and horizontal or vertical plane) and are being processed in parallel. How the software receives the data and performs its tasks is presented in chapter 5.

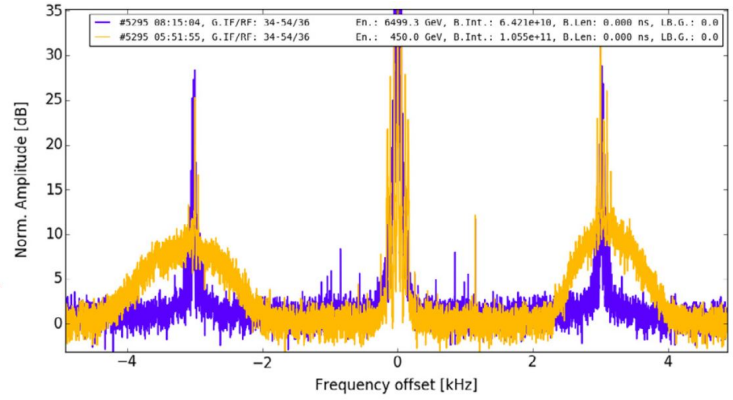

Figure 4.4: Typical Schottky spectra in the LHC for protons at injection (yellow, 450 GeV) and collision (blue, 6500 GeV). The area under the transverse sidebands scales with the emittance (the beam size), which reduces when the beam reaches higher energies above transition (section 2.2.3).

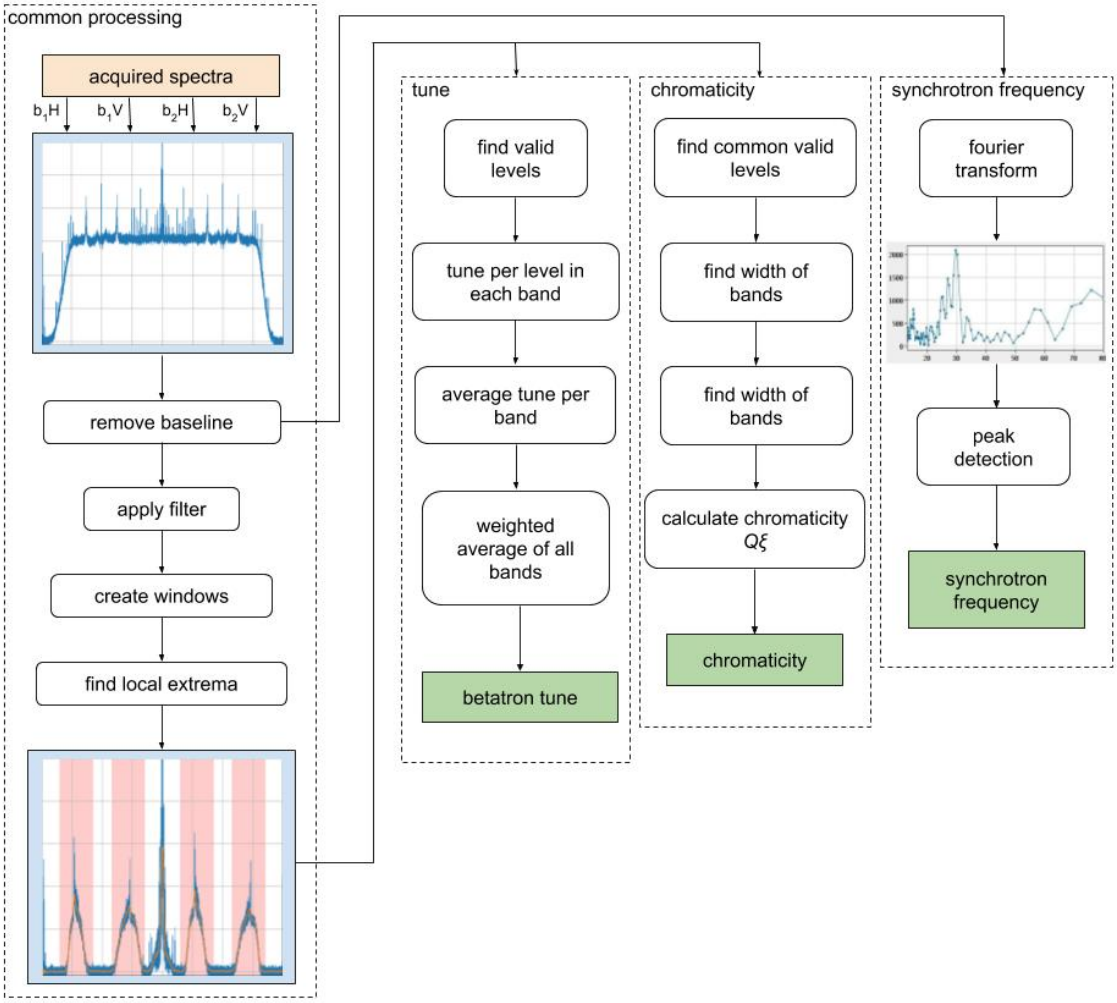

Figure 4.5: High level flowchart of the signal processing. After acquiring a spectrum from the BBQ class some common preprocessing steps are initiated, which then fires the subsequent parameter extraction methods.

4.2.1 Preprocessing

Before the estimation of the various beam parameters can take place, some digital preprocessing stages are required. These stages include: removing the baseline, low-pass filtering, location of the magnitude limits of each sideband.

The spectra acquired from the analog treatment chain has an intrinsic elevated noise floor due to unwanted common mode signals. The spectrum displayed just after acquisition in Fig. 4.5 shows an original spectrum with a baseline. The baseline is removed by using a reference spectrum that is obtained when there is no beam (or by turning off the front-end gating) to subtract from the spectra used for subsequent processing steps.

The measurements of parameters such as the betatron tune and chromaticity depend on the actual shape of the sidebands and are therefore affected by the presence of synchrotron lines/satellites and noise in general. This is why the subsequent measurement methods will be provided a pre-filtered spectrum. The filter is a simple moving average, Finite Impulse Response (FIR), filter with a custom window size that attenuates the unwanted signals for parameter measurements. The filtered signal is computed with a sliding window given by:

$$y[i] = \frac{1}{M} \sum_{j=0}^{M} x\left[i + j - \frac{M}{2}\right]$$

where x is the input signal, y is the output signal, and M is the number of points in the window.

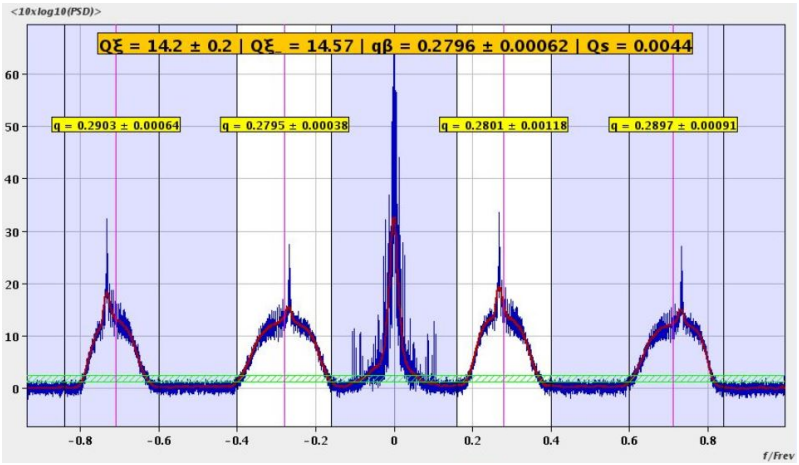

Figure 4.6: This view is given by the BQSChroma GUI that is currently available for operations. The white background around the transversal Schottky sidebands inherent to the Schottky harmonic revolution frequency is the sideband windows; the pink lines indicate each sideband's measured betatron tune q, while the yellow text boxes is the sidebands $\overline{q} \pm \sigma$; the green field is the area of valid common levels for calculating the width of the sideband; and the orange text field displays average chromaticity, chromaticity at the lowest valid level, tune and synchrotron tune (just like the betatron tune, the synchrotron tune is the synchrotron frequency normalized by the revolution frequency). The BQSChroma GUI will be further introduced in chapter 5.

The moving average performs a convolution of the input sequence x with a rectangular window of length M and height 1/M (normalizing the window) $\frac{1}{M}$. Since the signal analysis disregards the edges of the spectrum, the filter simply avoids the delay by filtering from $i = \frac{M}{2}$ to $i = M - \frac{M}{2}$.

To further narrow the computational processing scope, there are applied windows that cover each sideband. These windows are used not only for reducing the computational effort but also for removing unwanted spectral artifacts. Since the sidebands are symmetrical around the harmonic revolution frequencies, the user only needs to define a window for the upper sideband, which is then automatically converted to fit the other sidebands. There are some restraints to having a window that needs frequent changes due to the dynamic alterations in the beam shape. The main Schottky sideband displacement occurs when the beam is accelerated from injection to collision energy, as the tune working points changes (section 2.2.4) and transverse beam size decrease as a consequence the sidebands becomes narrower (section 2.2.3). This 'main' sideband displacement has been counteracted with two statistically optimized set of windows, that automatically changes between the two energy plateaus.

The last processing step that is common for both the tune and chromaticity measurement methods is finding the sidebands extremities, i.e. the lowest and highest power levels of the sideband. They must be carefully verified to make sure that they, in fact, belong to the sideband. The validation process is accomplished by:

1. finding an absolute min and max value inside the sideband window.
2. giving a range of uniformly spread levels between these absolute extremes.
3. having a sweeping mechanism that checks if any indices inside the absolute min and max crosses a level more than once for each side of the sideband.
4. the first and last level that are crossed only once for each side of the sideband is the valid extremities.

This sort of validation process will be repeated for both the tune and chromaticity methods, but with more dense level analysis. A simplistic step by step presentation of all the preprocessing steps:

Remove baseline In the original acquired spectra there is a large unwanted baseline present. By using a reference spectrum acquired when no beam is present in the accelerator, and subtracting it from all subsequent spectra, results in a measured spectrum with a flat baseline.

Low-pass filter Apply simple moving average filter with a custom window size to smooth the signal and remove unwanted artifacts. The red line in figure 4.6 is a moving average filter.

Window Define a distance from the center (0) to a beginning and end of a window, using the upper sideband as reference to create a universal window that will be converted to work for all sidebands. In figure 4.6 only the windows for the sidebands inherent to the Schottky harmonic revolution frequency is activated, this implies that the subsequent methods, that can extract information from all sidebands, only use these two. The white background represent the window from within the methods are being applied. After statistical analysis it has been created two default windows for injection energy and collision energy.

Locate extremities Find the valid extremities (lowest and highest values) of the sideband. What 'valid' suggests, is that the actual extremity is inherent to the sideband, since there might be adjacent extremes that actually are unrelated to the desired betatron sideband.

4.2.2 Betatron tune measurement method

In order to measure the betatron tune, a robust algorithm that should work for both injection and collision energy has been developed. Although one would think a peak-detecting algorithm would be sufficient to capture the coherent peaks centered on top of the transverse sidebands, the problem is that the strong coherent peaks are not always visible or perfectly centered (bands in Fig. 4.6 has coherent peaks that are astray from the actual center). What has been implemented is a method to find the average center for all active sidebands (active implies that they are being used for calculations, in Fig. 4.6 only the sidebands with a white background are active) and then do a weighted average of these averages to statistically estimate the most likely center.

The first thing the method does is to determine several valid levels and calculate a center at each of them. The level validation process is the same as for finding the local extremes in the preprocessing step. The only difference is that this step uses the resulting min and max valid levels from the preprocessing step as its own min and max for the sweep. When several valid levels are collected, the method measures the center between the indexes at every given level on each side of the sideband. These values are then averaged to acquire the mean tune $\overline{q}$ and variance σ^2 for each sideband.

The average of the estimated tunes for each sideband may not be the most likely tune since the sidebands might be displaced or deformed. The tune is estimated in the maximum likelihood sense by means of wheighting the various average tunes with the inverse of their variances σ^{-2}. The smaller the σ^2 the more likely the average is legitimate (because a higher variance implies a less uniform and dispersed average) [20]. Each tune and its weight is normalized by the sum of all weights:

$$\hat{q} = \frac{\sum_i \overline{q}_i \sigma_i^{-2}}{\sum_i \sigma_i^{-2}} \ , \tag{4.1}$$

where $\hat{q}$ is the most likely tune, $\overline{q_i}$ the average tune per sideband and σ_i^{-2} the inverted variance. By examining the sidebands' symmetry and their calculated ($q_i = \overline{q}_i \pm \sigma_i$) in Fig. 4.6, you can detect that the 2nd sideband has the most symmetrical body, and is thus given more weight (σ^{-2}). Here is a simplified step by step presentation of the betatron tune measurement process:

Valid limits Using the valid extremities from the preprocessing step as first and last magnitude values in a sweep across the sidebands using uniformly spread levels to locate valid levels that it can use to calculate center frequencies.

tune per level Measure a center between the valid x-axis values for each valid level for each sideband.

Average tune per sideband Calculate a mean $\overline{q_i}$ and variance σ_i^2 for the tunes of each sideband.

Most likely tune Using the σ_i^{-2} (an uncertainty estimation) as the weight of each sideband's average tune, one can calculate the most likely tune in the maximum likelyhood sense [20].

4.2.3 Chromaticity measurement method

The first step is to measure the widths of the sidebands, which now are the only missing components for applying Eq. 3.21 (from section 3.2.4) to calculate the chromaticity. This is possible as coefficients like the slip factor η and the Schottky harmonic n are constant, and we will use the tune that was calculated by the betatron tune measurement method in the previous section. Only the sidebands associated with the center harmonic ($f/f_{rev} = n$) are employed to estimate the widths $\Delta f_{lsb,usb}$.

Like with the tune measurement method, the widths are measured by using valid levels, but these levels have to be the same for both sidebands. This is because the method calculates a given chromaticity for each level, but if the levels do not match for both sides, Eq. 3.21 will not be valid. To make sure that we have valid levels for both sidebands, the beginning and end of the sweep is respectively set to the highest of the two sidebands lowest valid limit (from the reprocessing step) and the lowest of their highest valid limit. The last modification to the valid range is decreasing the upper limit by a relatively large fraction, since we are only interested in the widest points of the sideband, i.e. at the root of the sideband. The green horizontal field in Fig. 4.6 is the end result of a valid range from within valid levels are used to calculate chromaticities. After averaging the chromaticity for each valid level, we have achieved an estimation of the actual chromaticity and associated variance. A simpler step by step presentation of the chromaticity extraction method:

Common valid limits Find a common lowest and highest valid level, i.e. lowest level is set to the highest minimum of the two and highest level to the lowest maximum provided by the preprocessing. The highest level is reduced by a custom fraction, so that the sweeping field represents the base of the hump, since this is where the sidebands are at their widest and whose widths represents the frequency spread of the sidebands.

Measure widths Calculate the width of the valid levels found by the previous sweep within the valid field (within the green range on Fig. 4.6).

Calculate chromaticity ($Q\xi$) Use the widths of the sidebands to calculate a chromaticity for each valid level using equation 3.21. Average the chromaticities to approximate a most likely chromaticity $\overline{Q\xi}$.

While this averaging method is a robust technique to measure the chromaticity, it does not provide the absolute widest point of the sideband. Because of this, a more sensitive approach that utilizes the lowest valid level of the two (highest of both their minimum levels) to measure the chromaticity is running simultaneously. This method might in some cases give a more likely chromaticity, while the 'main' method will provide a more stable measurement. The first chromaticity $Q\xi$ inside the orange text field in Fig. 4.6 is the averaged chromaticity and the next the lowest level calculation.

4.2.4 Synchrotron frequency measurement method

As introduced in section 3.2.3, the distance between the Bessel lines in the longitudinal portion of the acquired frequency spectrum represents the synchrotron frequency, for instance in figure 4.7 the distance from the center ($p = 0$) to one of its adjacent lines ($p = -1$ or $p = 1$) in unit f_s/f_{rev} is 0.00445, which gives us a synchrotron frequency $f_s = 0.00445 \times frev = 50.04$ Hz.

If we treat the spectrum shown in 4.7 as an ordinary signal, the periodicity due to the synchrotron lines is clearly visible. Therefore, we can use Fourier analysis to detect the dominant periodicity in the power spectrum.

In order to optimize computational resources, the method uses a pre-defined area for which it analyses the periodicity of the spectrum, i.e. a window around the most coherent synchrotron lines like the ones in Fig. 4.7. Furthermore, it probes a limited number of pseudo-frequencies since we have a good idea of the range where the synchrotron frequency can be found. The magnitude of the spectrum at each pseudo-frequency, is provided by the DFT:

$$|A_f| = \sqrt{\left(\sum_{n=0}^{N} D_n e^{-if/N}\right)^2}, \tag{4.2}$$

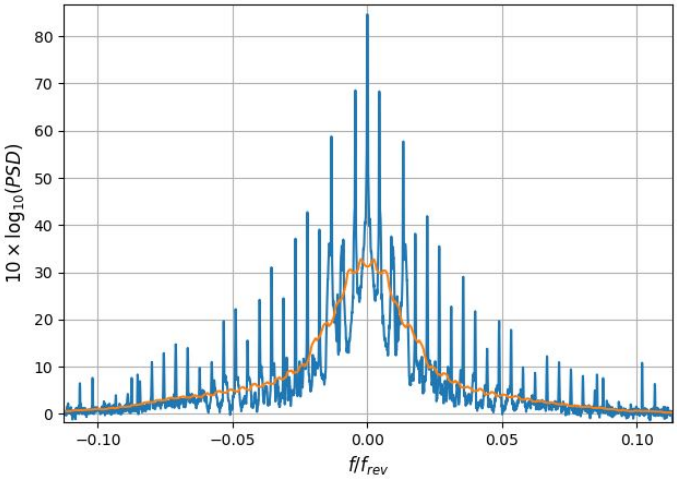

Figure 4.7: A closer look at a real example longitudinal Schottky signal. The blue line is unfiltered and orange the filtered signal.

where A_f is the magnitude of a given pseudo-frequency f, N is the total number of samples and D_n is the original spectrum power. For the DFT we use an conventional linearly spaced array of pseudo-frequencies to be probed:

$$f_k = f_0 + k\Delta f \ . \tag{4.3}$$

The only problem is that in the analysis of the results, we want to analyze the accumulated power for each pseudo-period, not pseudo-frequency. By inverting the frequencies we can create a corresponding pseudo-period axis, since $T = 1/f$:

$$T_s = f_k^{-1} = (f_0 + k\Delta f)^{-1} \ , \tag{4.4}$$

which is plotted in Fig. 4.8b. An example of the power of each pseudo-period (synchrotron frequency) in the new spectrum is shown in Fig. 4.8a. This exponential increase in step between probed synchrotron frequencies (pseudo-periods) implies less precision in the estimation of the dominant component for higher probing frequencies (pseudo-periods). In the future the probed synchrotron frequencies used for the DFT will be of an inverse exponential nature to cancel out this nonlinear behaviour.

To find the pseudo-period (synchrotron frequency) with the highest power, a simple peak detection method is applied. This will then be the most likely synchrotron frequency since the synchrotron lines should be the dominant fluctuation in the original longitudinal Schottky spectrum. In Fig. 4.8a the most likely synchrotron frequency is 52.8 Hz, i.e. a distance of $f/f_{rev} = f_s/f_{rev} \approx 0.00496$ in Fig. 4.7.

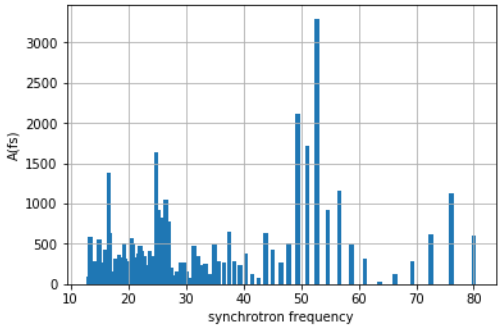

(a) Power Alevels of a given synchrotron frequency $f_s(k)$

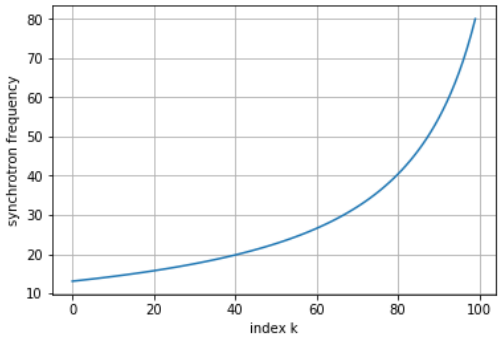

(b) f_s at each probe-index k

Figure 4.8: caption for both

A short step by step list for the synchrotron frequency measurement method:

Apply DFT Apply a DFT for a given window in the main spectrum. Create a defined synchrotron frequency probe range, but since this relates to the periods in the main spectrum, it has to be inverted to represent probing pseudo-frequencies for the DFT.

Representation of the DFT results After achieving the new spectrum, instead of the power being represented for the pseudo-frequencies used in the DFT, we want it to be represented for the pseudo-periods, which again is synchrotron frequencies $f_{s,k} = T_k = 1/f_k$

Peak detection Since the period with the most power (Fig. 4.8a) is the most likely synchrotron frequency, a simple peak detection method is used to find the line with the most power.

Chapter 5

Real-time software

In this chapter the real-time software that executes the digital signal processing steps introduced in the previous chapter is presented. The overwhelming majority of front-end software in Beams Department (BE) is designed, developed, deployed and maintained according to a standard comprehensive framework called Front-End Software Architecture (FESA). The FESA-based application (commonly referred to as a FESA class) developed for this project is called BQSAnalysis and comprises a sequence of real-time operations, appropriately scheduled, in order to perform the digital signal processing tasks described in the previous chapter. In addition, a dedicated JavaFX-based GUI has been developed in order to ease the real-time monitoring and control of the FESA class. Furthermore, the data is logged every 10 seconds to the LHC Logging Service where it is made accessible for off-line analysis through an interface called 'TIMBER'.

5.1 Architecture

5.1.1 FESA (Front-End Software Architecture)

The FESA is a framework used to develop real-time equipment software. The main reason for using this framework is to standardize, simplify and speed up the process of developing, deploying and integrating front-end software. The real-time software runs on a Front-End Computer (FEC) and can be used to control and monitor different types of equipments such as Programmable Logic Controllers (PLCs), power supplies or beam diagnostics. The developer produces three XML documents: Design, Deployment and Instantiation. The former two are used to generate device-specific C/C++ source code whereas the latter is the configuration file used by the FESA application at startup. A short overview of the three XML documents is listed below [21].

Class design: where the developer specifies which real-time actions are executed as a response to LHC timing events or custom user events. In addition, this is where the developer also pecifies the internal data structures and public interface. Upon validation, this document is used to generate generic source code on top of which the developer can add his/her user code. The result of this step is a library that later on will be linked in order to produce the final executable.

Deployment unit: where the developer specifies in which threads the real-time actions are to be executed. In the final compilation step, the code generated from this XML document is compiled and linked against the library generated in the previous stage in order to produce the final application executable.

Class instance: where the developer specifies the configuration parameters used at application startup.

Fig. 5.1 shows that operator/expert interactions/requests and real-time application behaviour are two complementary services that the developer has to model. The two are very different since the request-handling is driven by on-demand services while real-time accelerator events drive the timing system. Logically the request-handling should have a lower priority than the real-time events. Because of this, the two are decoupled by a shared software abstraction of the

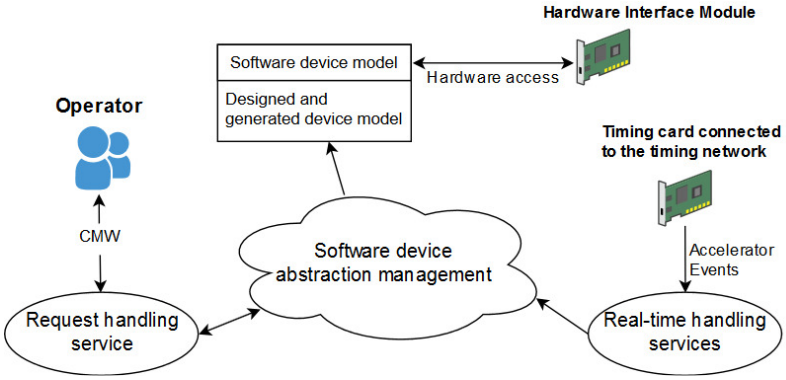

Figure 5.1: Separation of the *server* (operator side) and *real-time* layers. The complexity of the system and the communication with the device is managed by an software abstraction.

device model. This abstraction prohibits the user from accessing the device directly and instead makes it accessible through the so-called *server layer* [22].

The class design is split into two logical layers: *real-time* and *server*. The real-time layer is constantly running and is responsible for the communication between the FESA class and the hardware. It is managed by either internal logical events and/or externally triggered events. The server layer, however, provides a Controls Middleware (CMW) (common software communication infrastructure used in the CERN accelerator control system) interface for the user (can be an operator of the system or another FESA class) to be able to access it. It consists of a list of so-called properties that defines the data types that are remotely available for the user Operations such as SET, GET and MONITOR are readily available through CMW.

FESA also provides an automatically generated Java GUI known as a "FESA navigator", which allows access to every defined property of any declared device instance (section 5.2.2). There the user can set, get and monitor the class data while having the possibility to visualizing it in tables or plots.

5.1.2 Overview

The Schottky system is a collection of diverse parts working together, from the measured shot noise in the pick-ups all the way to the GUIs (Fig. 5.4). So far all the theoretical background, measurements and signal processing have been presented.

As shown in Fig. 5.4, the BQSAnalysis FESA class does not obtain the digitized signal directly from the ADC module at the end of the analog signal treatment chain, but from a FESA class called BBQ (short for BQBBQLHC) through the CMW. The ADC provides the BBQ class with 24-bit precision data at a sampling frequency $f_s = 4f_{rev} = 44982$ kHz (section 4.1). It uses data sets of length $N_{FFT} = 2^{16} = 65536$ to perform the Fast Fourier Transform (FFT), which suggests that it should be able to provide a frequency spectrum every $N/f_s = 1.4525$ seconds. However, the BBQ class publishes a new spectrum, through CMW, every second. Because of this difference in the rate of ADC data accumulated and frequency spectra provided, the BBQ class copies the the last $0.4525 \cdot f_s \approx 20354$ values in the previous ADC data set and combine it with the next 0.5475 seconds worth of new data (notice the overlap of the data sets in Fig. 5.3). After it has calculated the FFT, the spectrum looks like the one in Fig. 5.2. The ratio between the power of the longitudinal center frequencies and the sidebands can be of the order of 10^5. For visualization purposes, it is therefore convenient to display the in a dB scale:

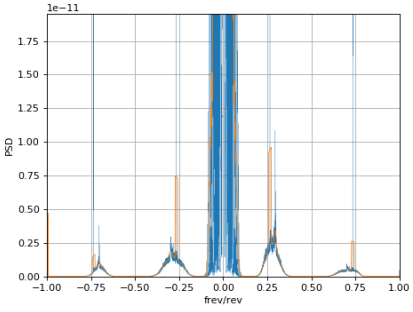

Figure 5.2: Example of a Schottky PSD

$$PSD_{db}(f) = 10 \times log_{10}(PSD(f)) \ . \tag{5.1}$$

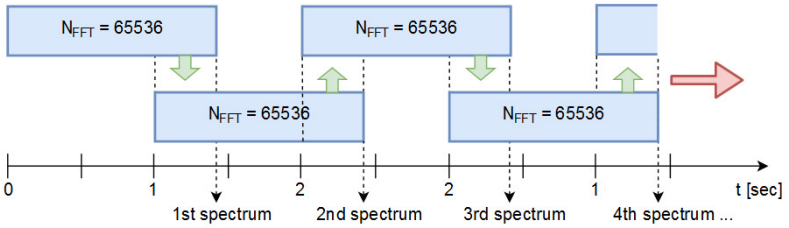

Figure 5.3: The BBQ FESA class publishes 16bit frequency spectra to the CMW every second, but it takes 1.45 seconds to receive this amount of data form the ADC. What it does is to copy (green arrow) 0.45 seconds worth of data from the previous data set and combines it with the next 0.55 seconds to use for frequency analysis.

The published spectrum is averaged (using an exponential moving average[23]) in order to reduce noise and artifacts according to:

$$\widehat{PSD}_{db,i}(f_k) = \alpha PSD_{db,i}(f_k) + (1-\alpha)\widehat{PSD}_{db,i-1}(f_k) \ , \tag{5.2}$$

where α is the smoothing factor, $PSD_{db,i}(f_k)$ is the power at frequency f_k at discrete time instant i, $\widehat{PSD}_{db,i-1}(f_k)$ is the power estimate at frequency f_k for discrete time instant $i-1$ and $\widehat{PSD}_{db,i}(f_k)$ is the power estimate at frequency f_k for discrete time instant i. The smoothing factor is usually $\alpha \approx 0.02$, which suggests that there will be a delay before the spectrum responds to a sudden modification of machine parameters.

While processing the data, the BQSAnalysis class is periodically publishing the results in the form of 'acquisition properties' that can be read from either the FESA navigator GUI or the BQSChroma GUI.

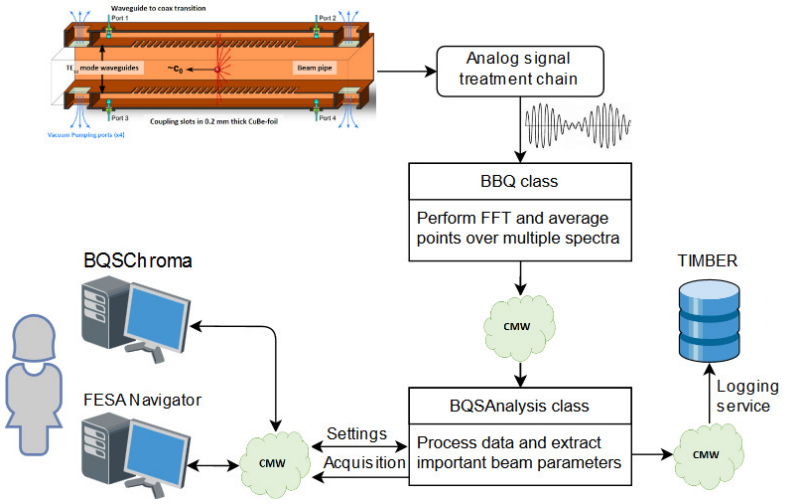

Figure 5.4: Flowchart of the whole system all the way from the Schottky pick-ups in the LHC to the user interfaces

In addition to the real-time visualization tools, the data is logged in the LHC logging database and made accessible through a Java Web application GUI called "TIMBER". The user selects FESA variables of interest to be recorded. The user can later select the data within a time range, and either see a statistical summary, visualize it in an interactive chart or extract it to a file for complementary off-line analysis [24].

5.2 BQSAnalysis FESA class

Now that the FESA architecture has been introduced and an overview of how the software receives and distributes its data has been presented, we can explore the internal structure of the BQSAnalysis class. The BQSAnalysis subscribes to 4 , the Schottky spectra for LHC beam 1 horizontal,

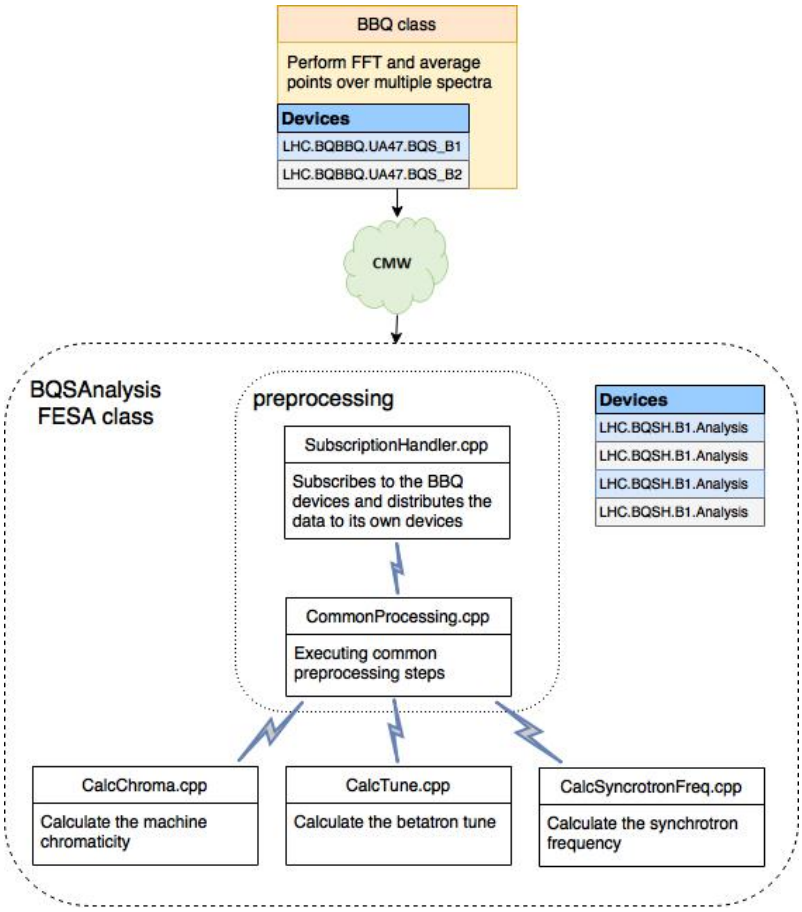

Figure 5.5: Overview of the BQSAnalysis FESA class

beam 1 vertical, beam 2 horizontal and beam 2 vertical. The processing of each of these spectra is replicated over 4 so-called devices. All the Digital Signal Processing (DSP) functions presented in section 4.2 are implemented as different real-time actions. These operations are executed in a sequential order within a single device[1].

5.2.1 Real-time actions

The SubscriptionHandler is the first real-time action in the sequence and is notified whenever a subscription event occurs. When the BBQ publishes new spectra thorugh CMW, the subscription handler iterates through the devices and copies the data fields to local buffers (see the different devices received for both FESA classes in Fig. 5.5). In the class design XML document (section 5.1.1) the completion of the SubscriptionHandler action triggers the start of the CommonProcessing action. The triggering of subsequent real-time actions is shown in Fig. 5.5 as a communication link (lightning).

The code in CommonProcessing corresponds to the preprocessing pseudo code in section 4.2.1. When CommonProcessing completes, it triggers the CalcChroma, CalcTune and CalcSynchrotronFreq real-time actions simultaneously. The methods used for calculating these parameters were also treated in the previous chapter in section 4.2.

5.2.2 Interfaces

In the design XML document acquisition and settings properties have been created for each real-time action. In these properties, referenced data fields are exposed. As mentioned before, FESA also provides an automatically generated Java GUI that provides access to all properties for all devices of the FESA class. It handles different commands while providing tools to visualize the

[1] but in parallel across devices.

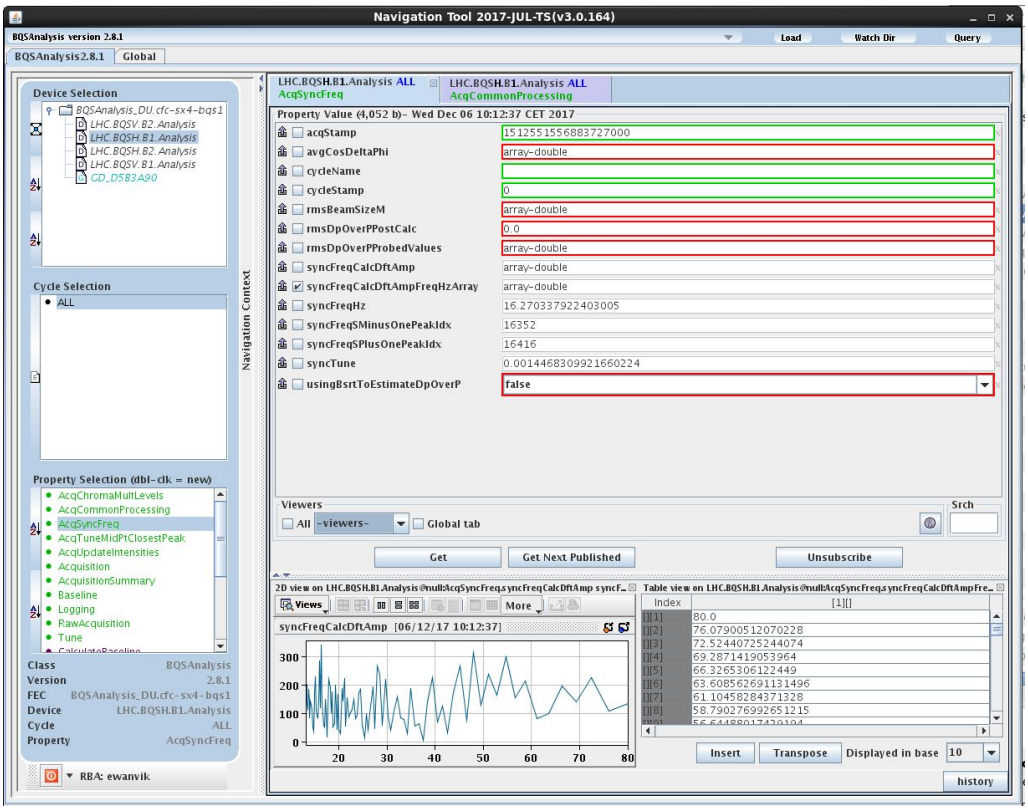

Figure 5.6: The FESA navigator

either as a custom plots or tables. Fig. 5.6 shows the FESA Navigator for the BQSAnalysis FESA class, where you can for instance:

- choose a device to be examined (top left)
- select cycle (the LHC only has one cycle)
- select properties (bottom left) to be shown in separate tabs
- execute commands like get, set and subscribe.
- choose different modes to display the data fields, e.g. a table or 2d plot.

In Fig 5.6 the synchrotron acquisition property has been selected and is the currently active tab. The navigator is subscribing to the property, which implies that the values are updated whenever the property is notified. At the bottom of the Navigator is a 2D plot showing the synchrotron frequency and a table showing the probed synchrotron frequencies. These values are taken from the same source as depicted in Fig. 4.8 in section 4.2.4, but since the snapshot is taken after the 2017 winter-shutdown there are no beams and thus the poor synchrotron frequency measurements.

5.3 BQSChroma GUI

The BQSChroma GUI was briefly introduced in section 4.2, where Fig. 4.6 shows a snapshot of the display for beam 1 in the horizontal plane. The BQSChroma GUI is a desktop application created using JavaFX. The comprehensive display contains information from all four devices in the BQSAnalysis FESA class: the left column is beam 1 and right is beam 2, while upper row is for the horizontal plane and the lower for the vertical. The snapshot in Fig. 5.7 shows the pre-processed frequency spectra; the baseline has been removed, the blue line is the raw spectrum, the red is the filtered spectrum and the white area represents the sideband windows. In each spectrum, the position of the calculated average tune for each sideband is illustrated as a pink line, while the yellow text boxes are the sideband's $\bar{q} \pm \sigma$. The green field is the area of valid common levels for measuring the widths of the sidebands used for calculating the chromaticity. At the top of each display is an orange text field that shows the average chromaticity using multiple

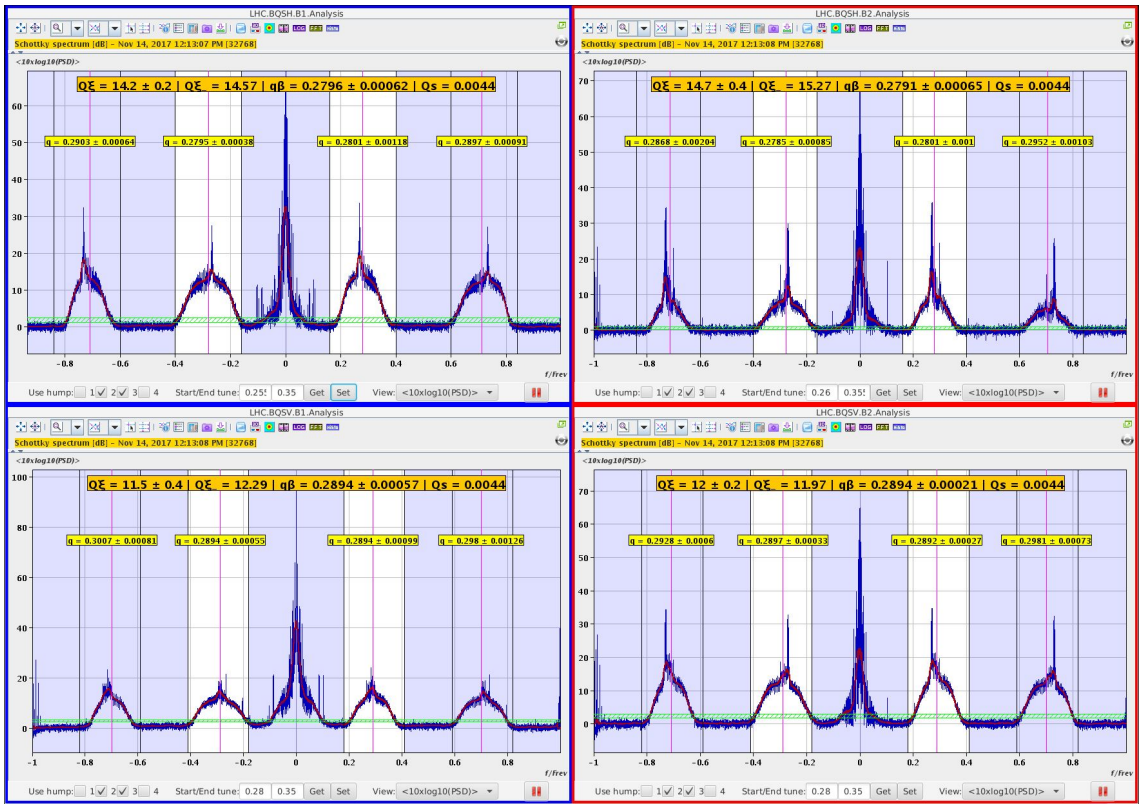

Figure 5.7: The BQSChroma GUI

levels, chromaticity at the lowest valid level, average betatron tune and the synchrotron frequency normalized by the revolution frequency ($Q_s = f_s/f_{rev}$). The units of the x-axis is normalized frequency f/f_{rev}. Because of the logarithmic scale and exponential moving average (section 5.1.2) the y-axis in Fig. 5.7 is given in $\langle 10 \times log_{10}(PSD) \rangle$ (the angle brackets denote averaging in time, in this case this corresponds to the exponential moving average). The toolbar at the bottom of each display is where the operator can: choose which sidebands to use for parameter calculations (2 and 3 are active in Fig. 5.7), set the windows and choose different plot views.

In addition to the "spectrum view" used in Fig. 5.5, the GUI can also display historical plots of the tune, chromaticity and synchrotron frequency calculations. An example of a plot of the chromaticity estimates as a function of time is shown in Fig. 6.2 in the next chapter.

Chapter 6

Results and conclusions

In this chapter the results obtained for the measurement of each of the 3 parameters (chromaticity, betatron tune and synchrotron frequency) is discussed. These are preliminary results as the measurement system is still in an early stage of validation.

An implementation that is worth mentioning before presenting the results of the measurement methods is the automatic change in sideband window between injection and collision energy. In the early stages of the deployed software, the system depended on manual setting of the computational windows (white backgrounds Fig. 6.1). This dependence on the operator changing the windows often resulted in inadequate real-time measurements. One simple change was to automatize the alternation between optimal window settings for injection and collision energy. These automatic window settings were estimated based on an analytic analysis of spectra logged during previous LHC fills to determine the best sideband coverage while avoiding the adjacent unwanted artifacts.

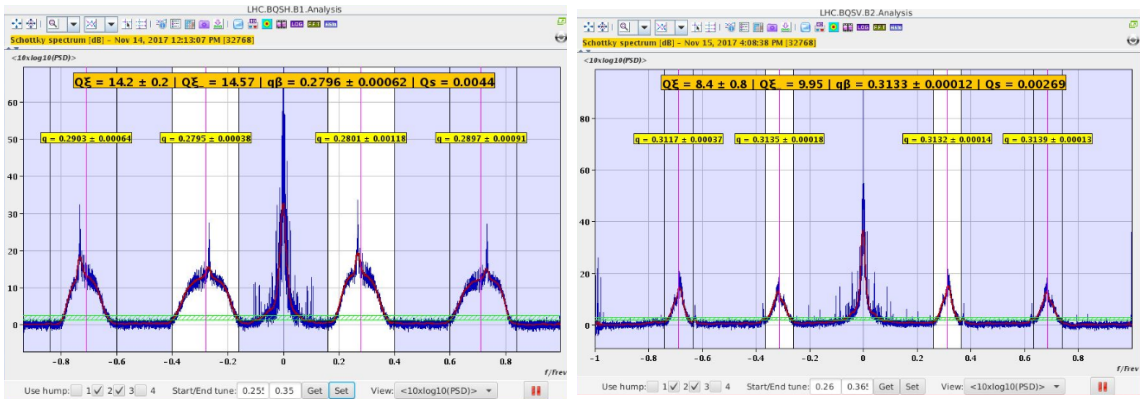

(a) Injection energy **(b)** Collision energy

Figure 6.1: Beam1 horizontal frequency spectrum, before and after acceleration. The decrease in total power as a consequence of lower beam size is visible.

6.1 Chromaticity

There was a recent Machine Development (MD) (i.e. dedicated experiment) for validating the chromaticity measurements provided by the LHC Schottky system that took place on December 1, 2017. During this experimental session, sextupole magnets were used to obtain approximate[1] chromaticity set-points within the range $-3 < Q\xi < 20$. These set-points and the time at which they occurred were recorded and used to provide an indication of the quality of the chromaticity measurement using the Schottky system. The use of RF modulation method for measuring chromaticity has to be kept to a minimum due to the particle losses it causes. During the experimental

[1] the sextupole magnets were driven in feed-forward mode based on theoretical modelling hence the exact chromaticity was not actually measured.

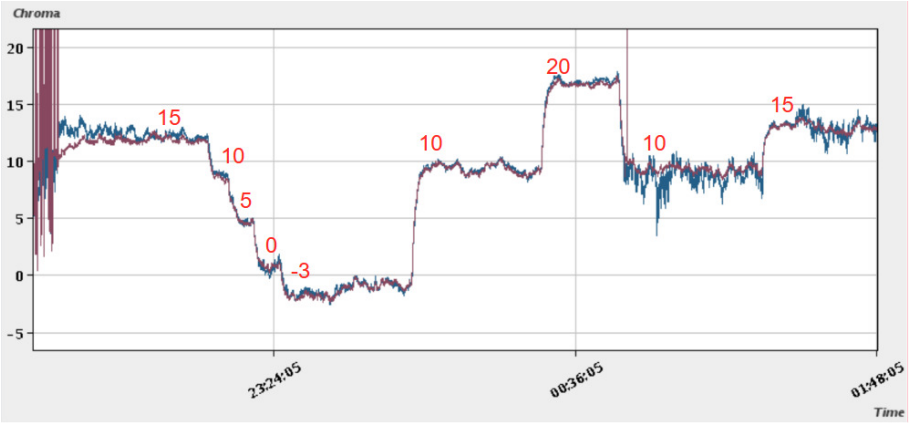

Figure 6.2: Result of the chromaticity measurements during the recent MD

session this method was used 3 times to confirm the chromaticity set-points. This was introduced in section 2.3.1, see [12] for further information. Fig. 6.2 shows the chromaticity measured with the BQSAnalysis FESA class for beam 2 in the vertical plane. As introduced in section 4.2.3, there are two methods in use for calculating the chromaticity: one using an average of several valid levels and the other using the lowest common level. In Fig. 6.2 the burgundy line is the averaged chromaticity and blue is the chromaticity at the lowest level. The sequence of the chromaticity targets during the MD is shown in table 6.1.

A varying offset between the chromaticity measurements and the theoretical set-points has been observed. This offset seems to scale with the absolute value of chromaticity. The smallest deviation is observed for chromaticity values around +5 and increase in both positive and negative directions. The largest offset is observed at a set-point of 20. At around 22:41 (theoretical chromaticity set-point of +15) the Schottky measurement seems to agree with the traditional RF modulation measurement.

22:12	chromaticity set to 15	**23:54**	RF modulation measured -2.4
22:41	RF modulation measured 12.6	**23:56**	chromaticity set to 10
23:08	chromaticity set to 10	**00:00**	RF modulation measured 11.2
23:13	chromaticity set to 5	**00:28**	chromaticity set to 20
23:19	chromaticity set to 0	**00:46**	chromaticity set to 10
23:25	chromaticity set to -3	**01:22**	chromaticity set to 15

Table 6.1: Chromaticity during Schottky Machine Development (MD)

Fig. 6.3 displays a historical plot of both chromaticity measurement methods at injection and collision energies. During non-stationary beam phases, i.e. acceleration, the Schottky spectra become complex and virtually impossible to analyze. As introduced in section 2.2.3 and shown in Fig. 4.4, there is a decrease in geometric emittance (beam size), which corresponds to the total power in the sidebands (thus effectively lowering the signal-to-noise ratio). This makes it more difficult to extract information from the sidebands and makes the measurements less accurate.

Although there were discrepancies during the MD, the results are satisfactory. An example of why the averaging method (burgundy line) is a more robust approach appears after the change in set-point from 20 to 10 chromaticity at 00:46 in Fig. 6.2, where the lowest level chromaticity method (blue line) is clearly noisier. There are still room for improvements and these methods will work as a foundation for more complex techniques in the future. In section 6.4 a new chromaticity measurement method that is currently under development will be introduced.

6.2 Betatron tune

To evaluate the performance of the betatron tune measurement method, it is compared with the traditional LHC tune measurement system "Base-Band-Tune" BBQ (Fig. 6.4). The BBQ FESA

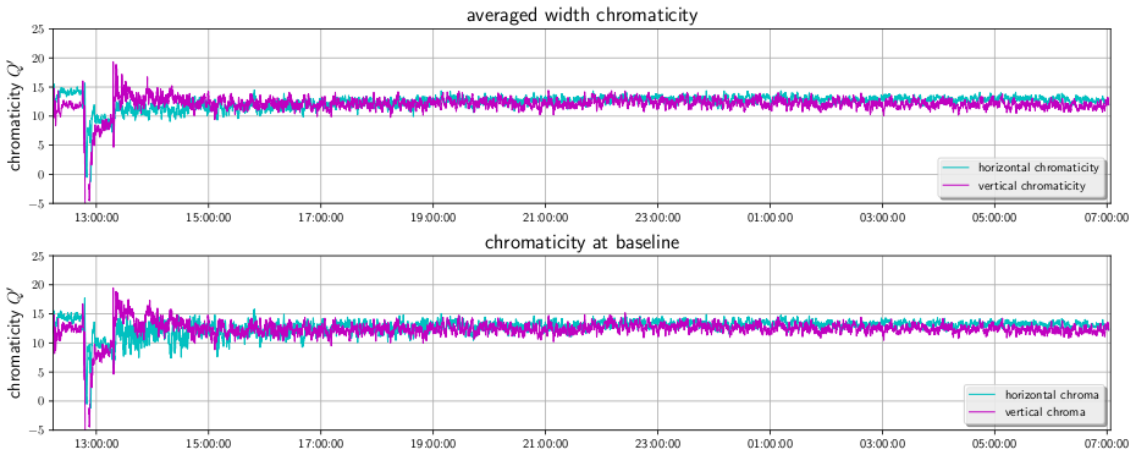

Figure 6.3: Chromaticity measurements from fill 6399. It lasted until 04.00, but is shortened to highlight the effects of the acceleration from injection (450 GeV) to collision energy (6.5 TeV) (from 12:41-12:45). The automatic window does not kick in before after the acceleration is done.

class was introduced in the overview of the Schottky system in section 5.1.2. Note that the BBQ system operates at a measurement rate of 10 Hz (light gray trace) and has a strong variance. To reduce this, the signal was averaged over a 10 second period, to achieve a more reliable comparison. Alike chromaticity, there are poor tune measurements during the energy ramp, but it stabilizes when the automatic window adjustment is triggered. In Fig. 6.4 the ramp starts at 22:13 and the windows adjustments appears when the ramp is done at 22:22.

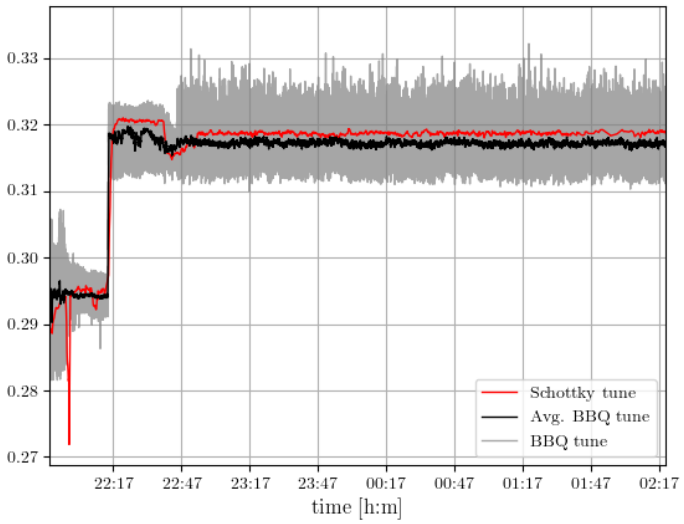

Figure 6.4: Schottky tune method measurements compared to the traditional BBQ tune measurement over time. Both a 10 second moving average and the original BBQ signal is shown.

Again, as with the chromaticity, the betatron tune method gave satisfactory results. It is supposed to be a stable technique and act as a foundation for future improvements. The performance of the method is stable and produces satisfactory measurements at both injection and collision energy.

6.3 Synchrotron frequency

The method of measuring the synchrotron frequency was introduced in section 4.2.4. Under original LHC design conditions, the synchrotron frequency is supposed to be 61.8 Hz at injection energy and 21.4 Hz at collision energy according to the "LHC Design Report" [5]. It is acknowledged by operator physicists that at injection energy the synchrotron frequency is around 52 Hz and around 21 Hz at top energy.

During the MD the energy ramp started at 02:14, which in Fig. 6.5 is made apparent by the decrease in synchrotron frequency. There is a small delay in the response due to the exponential moving average performed by the BBQ FESA class.

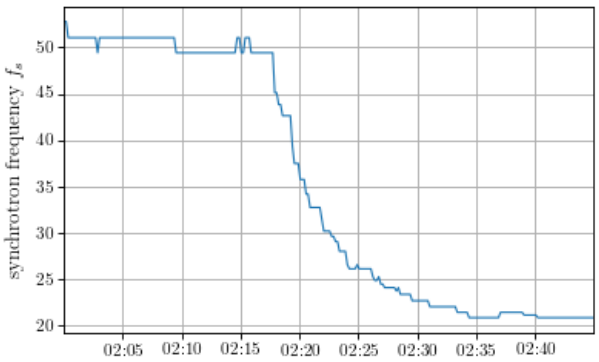

Figure 6.5: Synchrotron frequency measurements during acceleration from injection to collision energy

The method to measure the synchrotron frequency using a periodic analysis of the spectra has produced impressive results. However, there are still a few things that need to be changed. One example is the exponential increase in distance between the probed frequencies for the DFT, which is visible in both plots in Fig. 4.8. This increasing frequency probe width reduces the precision for estimating higher synchrotron frequencies. To achieve a linear spread in the synchrotron frequencies given by Eq. 4.4, it is possible to invert the frequency probes in Eq. 4.3.

6.4 Future work

In an effort to improve the accuracy of the Schottky-based measurements, a new method is being tested on previously logged spectra. The principle of this method is essentially to analyze the power of individual synchrotron satellites in the sidebands. The theoretical background for this method stems from Eq. 3.19 after generalizing it to the case of a particle ensemble (bunch) instead of a single particle-based treatment. In order to assess and further develop this new method, a dedicated GUI (see Fig. 6.6) has very recently been developed using the python programming language.

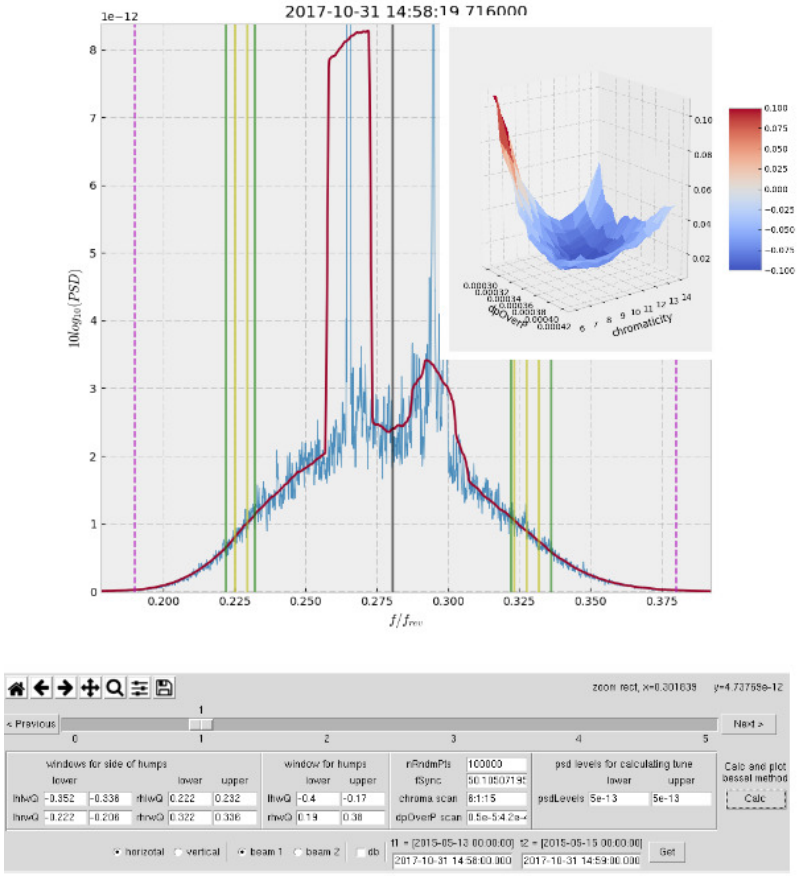

Figure 6.6: GUI used to assess and further develop a new method to measure chromaticity

Bibliography

[1] F. Caspers, "Schottky signals for longitudinal and transverse bunched-beam diagnostics," 2009. https://cds.cern.ch/record/1213284.

[2] CERN, "How a detector works." https://home.cern/about/how-detector-works, 2012.

[3] CERN, "About CERN." https://home.cern/about, 2012.

[4] P. J. Bryant, "A brief history and review of accelerators," 1994. https://cds.cern.ch/record/261062.

[5] O. S. Brüning, P. Collier, P. Lebrun, S. Myers, R. Ostojic, J. Poole, and P. Proudlock, *LHC Design Report*. CERN Yellow Reports: Monographs, Geneva: CERN, 2004. https://cds.cern.ch/record/782076.

[6] CERN, "Pulling together: Superconducting electromagnets." https://home.cern/about/engineering/pulling-together-superconducting-electromagnets, 2012.

[7] CERN, "Accelerators." https://home.cern/about/accelerators-topics, 2012.

[8] CERN, "Experiments." https://home.cern/about/experiments, 2012.

[9] CERN, "Lorentz Force." https://www.lhc-closer.es/taking_a_closer_look_at_lhc/0.lorentz_force, 2012.

[10] S. Baird, "Accelerators for pedestrians; rev. version," Tech. Rep. AB-Note-2007-014. CERN-AB-Note-2007-014. PS-OP-Note-95-17-Rev-2. CERN-PS-OP-Note-95-17-Rev-2, Feb 2007. https://cds.cern.ch/record/1017689.

[11] CERN, *CERN Accelerator School - Magnets*, (Geneva), CERN, 2010. https://cds.cern.ch/record/1158462. 14 lectures, 494 pages, published as CERN Yellow Report http://cdsweb.cern.ch/record/1158462.

[12] R. J. Steinhagen, "Tune and chromaticity diagnostics," 2009. https://cds.cern.ch/record/1213281.

[13] E. W. Weisstein, "Maclaurin Series." http://mathworld.wolfram.com/MaclaurinSeries.html. From MathWorld–A Wolfram Web Resource.

[14] S. Guiducci, "Chromaticity," p. 16 p, Jun 1991. https://cds.cern.ch/record/223348.

[15] A. Jeff, A. Boccardi, E. Bravin, A. Fisher, T. Lefevre, A. Rabiller, F. Roncarolo, and C. P. Welsch, "First results of the LHC longitudinal density monitor," *Nucl. Instrum. Methods Phys. Res., A*, vol. 659, pp. 549–556. 8 p, Aug 2011. https://cds.cern.ch/record/1395374.

[16] D. Boussard, "Schottky noise and beam transfer function diagnostics," 1989. https://cds.cern.ch/record/1542461.

[17] E. W. Weissttein, "Bessel Function of the First Kind." http://mathworld.wolfram.com/BesselFunctionoftheFirstKind.html. From MathWorld–A Wolfram Web Resource.

[18] M. E. Castro Carballo, *Transverse diagnostics for high energy hadron colliders*. PhD thesis, Santiago de Compostela U., 2007. http://weblib.cern.ch/abstract?CERN-THESIS-2008-040.

[19] M. Betz, O. Jones, T. Lefevre, and M. Wendt, "Bunched-beam schottky monitoring in the lhc," *Nuclear Instruments and Methods in Physics Research Section A: Accelerators, Spectrometers, Detectors and Associated Equipment*, vol. 874, no. Supplement C, pp. 113 – 126, 2017. http://www.sciencedirect.com/science/article/pii/S0168900217309452.

[20] *Weighted Arithmetic Mean*, pp. 565–566. New York, NY: Springer New York, 2008. https://doi.org/10.1007/978-0-387-32833-1_421.

[21] M. Arruat, J. J. Gras, A. Guerrero, S. Jackson, M. Ludwig, and J. L. Nougaret, "CERN Front-End Software Architecture for Accelerator Controls," p. 4 p, Nov 2003. https://cds.cern.ch/record/693143.

[22] the FESA team at CERN, "FESA Essentials," tech. rep., CERN, 2004. http://project-fesa.web.cern.ch/project-fesa/binaries/documents/FesaEssentialsBundle.pdf.

[23] G. Upton and I. Cook, "exponential smoothing." http://www.oxfordreference.com/view/10.1093/acref/9780199541454.001.0001/acref-9780199541454-e-578.

[24] R. Billen and C. Roderick, "The LHC Logging Service: Capturing, storing and using time-series data for the world's largest scientific instrument," Tech. Rep. AB-Note-2006-046. CERN-AB-Note-2006-046, CERN, Nov 2006. http://cds.cern.ch/record/1000757.